






Heuristic estimation of river bathymetry in braided streams using digital image processing

Davide Mancini¹  | Gilles Antoniazza¹  | Matteo Roncoroni²  |
François Mettra¹  | Stuart N. Lane¹ 

¹Institute of Earth Surface Dynamics (IDYST),
Université de Lausanne (UNIL), Lausanne,
Switzerland

²Eau Terre Environnement Research Centre,
Institut National de la Recherche Scientifique
(INRS), Québec City, Canada

Correspondence

Davide Mancini, Institute of Earth Surface
Dynamics (IDYST), Université de Lausanne
(UNIL), Lausanne, Switzerland.
Email: davide.mancini@unil.ch

Funding information

Swiss National Science Foundation (SNSF),
Grant/Award Number: 200021_188734

Abstract

Measurement of river bathymetry has been revolutionized by high-resolution remote sensing that combines UAV platforms with SfM-MVS photogrammetry. Mapping inundated and exposed areas simultaneously are possible using either two-media refraction correction or some form of the Beer-Lambert Law to estimate water depths. If, as in turbid glacially-fed braided streams, the bed is not visible then traditional survey techniques (e.g. differential GPS systems) are required. As an alternative, here we test whether the spatial distribution of water depths in a shallow braided stream can be modelled from basic planimetric data and used to estimate inundated zone bathymetry. We develop heuristic rules using; (1) distance from the nearest river bank; (2) total inundated width along a line tangential to the local flow direction; (3) local curvature magnitude and direction; and distance from the nearest flow (4) divergence and (5) convergence regions. We parameterize them using a sample of measured water depths in stepwise multiple linear regressions and validate them using independent data. Resulting water depth distribution maps explain between 50% and 60% of the measured water depth spatial variability when compared to independent data. After incorporating modelled water depths into digital elevation models (DEMs) of exposed areas, we show that the developed method is suitable for volumetric change calculations in both dry and inundated areas.

KEYWORDS

bathymetric mapping, multiple linear regression, SfM-MVS photogrammetry, stepwise regression, turbid proglacial streams

1 | INTRODUCTION

River bathymetry is an important parameter in fluvial geomorphology for both geomorphological and ecosystem processes (Lane et al., 2010; Ward et al., 2002; Woodget et al., 2015). Its accurate measurement allows for quantitative detection of river channel changes through time (Lane et al., 2003; Westaway et al., 2003); better understanding of fluvial systems through hydraulic modelling (Lane et al., 2020); physical habitat assessment and river restoration (Maddock, 1999) and sediment budgeting studies (Hicks, 2012; Marcus et al., 2012).

The 1990s saw the first attempts (Lane et al., 1994) to represent river bathymetry as a continuous surface (i.e. Digital Elevation Models or DEMs) rather than a series of cross-sections. They relied upon interpolation of point data acquired using differential GPS (e.g. Brasington et al., 2000) or total stations, sometimes aided by terrestrial analytical photogrammetry for exposed areas (e.g. Chandler et al., 2002; Lane et al., 1994). Such field surveys are extremely time-consuming and lead to a trade-off between spatial resolution, spatial extent and the frequency of resurvey that directly impacts the quality of the results that are acquired (Lane, 1998). They also require physical contact with the riverbed (e.g. walking in the river) potentially

This is an open access article under the terms of the [Creative Commons Attribution-NonCommercial-NoDerivs](https://creativecommons.org/licenses/by-nc-nd/4.0/) License, which permits use and distribution in any medium, provided the original work is properly cited, the use is non-commercial and no modifications or adaptations are made.

© 2024 The Author(s). *Earth Surface Processes and Landforms* published by John Wiley & Sons Ltd.

modifying it; and are limited to wadeable areas at high flows (Bangen et al., 2014; Kasvi et al., 2019; Marcus & Fonstad, 2008). The ease with which bathymetric mapping can be undertaken is thus much more limited compared to the measurement of dry areas (Brasington et al., 2000; Westaway et al., 2003).

Developments in remote sensing, initially based upon the depth signature in airborne optical imagery (Gilvear et al., 1995, 1998), and eventually using multispectral (e.g. Legleiter et al., 2004; Legleiter & Roberts, 2005; Winterbottom & Gilvear, 1997) and hyperspectral (e.g. Marcus et al., 2003) imagery, addressed this limitation. The development of digital photogrammetric analysis for airborne imagery increased the feasibility of photogrammetric-based approaches allowing for much larger spatial extents. Westaway et al. (2000, 2001) provided a fully photogrammetric solution based upon two media refraction corrections for inundated zones where riverbed texture could be identified on the stream bed. Using airborne imagery, Westaway et al. (2003) showed that it was possible to combine water depths derived from optical imagery for inundated zones with photogrammetric data from exposed areas to provide very high resolution (< 0.5 m), good precision (ca. ± 0.2 to ± 0.3 m) data over a large extent of braided river (3 km \times 1.5 km). This required field calibration of the relationship between depth and spectral signature but Lane et al. (2010) showed that this method could be adapted for archival data where no calibration data were available.

Up until the 2010s, these approaches were limited by the cost of airborne imagery. This was revolutionized by the growing availability of low-cost Uncrewed Airborne Vehicles (UAVs) coupled with Structure-from-Motion Multi-View-Stereo (SfM-MVS) photogrammetry (Eltner et al., 2015; Hugenholtz et al., 2013; James et al., 2020; Niethammer et al., 2010; Ouedraogo et al., 2014). High vertical precision (ca. ± 0.05 - ± 0.2 m) and high resolution (ca. 0.01 to 0.1 m) data can now be acquired for rivers at a frequency dictated by the rate of morphological change rather than limited by the costs of data acquisition producing accurate DEMs of dry areas. The extension of two media refraction corrections to UAV-derived data allows the reconstruction of water depths and so production of models for both inundated and dry zones (Dietrich, 2017). The possibility of combining these two techniques represents a significant development in fluvial geomorphology, although subsequent research has identified limitations. Notably, the low-grade cameras in many UAVs make camera calibration challenging for reliable change detection (Carbonneau & Dietrich, 2017; James et al., 2020; James, Robson, d'Oleire-Oltmanns, & Niethammer, 2017; James, Robson, & Smith, 2017).

One major challenge remains: where rivers have high turbidity, water depths may exceed the maximum depths that can be seen in aerial imagery (i.e. the extinction depth). This may make the riverbed insufficiently visible for the application of texture-based two-media photogrammetry approaches for water depth modelling (e.g. Dietrich, 2017; Flener, 2013; Flener et al., 2013; Kasvi et al., 2019; Tamminga et al., 2015). Light extinction depth measured using Secchi depths may be of the order of only a few centimetres in certain fluvial settings (Carrivick & Heckmann, 2017) eliminating the depth signature for image-based approaches. Green-band lidar typically only penetrates to 1.5 to 3 times the Secchi depth (Pratomo et al., 2019; Szafarczyk & Tos, 2023), limiting the suitability of airborne lidar for bathymetric measurement in high-turbidity rivers. Other active remote sensing techniques exist, including

echo-sounding and acoustic Doppler current profiling. These perform better in high turbidity environments, but they cannot be used in water depths lower than 0.3 m to 0.5 m, limiting their application to large rivers (Kasvi et al., 2019).

Large-scale measurements suggest basic relationships between planform morphological properties (notably channel width) and water depth (Almeida et al., 2017; Mersel et al., 2013; Schaperow et al., 2019). Such relations are implicit in the long-established notion of hydraulic geometry (Leopold & Maddock, 1953) that allows stream widths, mean depths and mean velocities to be predicted from discharge. Such relationships were developed primarily for morphologically stable, single-channel streams. Bures et al. (2019) used linear multiple regression to predict cross-section bathymetry using morphometric data (i.e. overall curvature, planar curvature, profile curvature, overall slope and slope in the x- and y-direction). Interpolation between cross-sections was then applied to obtain a complete bathymetry of a meandering river.

In this paper, we estimate water depth distribution in a high turbid, braided, glacier outwash stream from basic planimetric information and assess its potential for creating DEMs for volume change estimation. The approach is based on a heuristic argument, which is a set of qualitative statements of how we expect water depth to vary in a braided river. We then transform these into quantitative, statistical models for generating spatially continuous water depths in inundated zones. We then (1) integrate these depths into high-resolution SfM-MVS derived topographic data from dry areas to create DEMs; and (2) assess whether they can be used for geomorphic change detection and volume estimation at the proglacial floodplain scale.

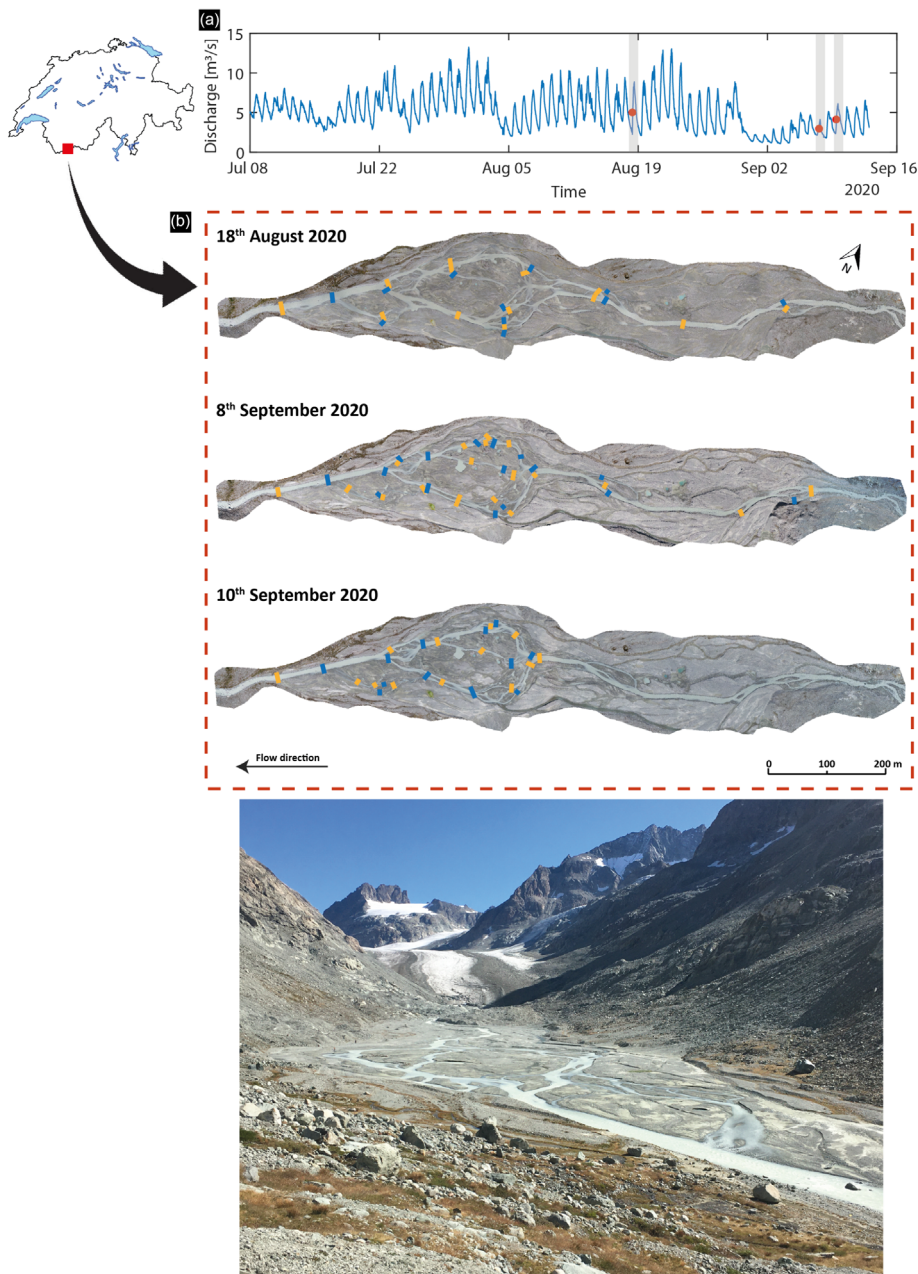
2 | METHODOLOGY

2.1 | Study area

The investigation is based on the proglacial margin of the Glacier d'Otemma, located at an altitude of 2,450 m a.s.l. in the Val de Bagnes, south-western Swiss Alps (Figure 1). This includes a glacial outwash plain that has formed between the early 1980s and the present following rapid glacier retreat (Mancini & Lane, 2020). The outwash plain varies between ca. 150 and 200 m wide and is just over ca. 1 km in length. There is no vegetation cover except on lateral terraces that are outside of the active braiding zone. The river has a median grain-size (D_{50}) of ca. 0.06 m and with surface particle sizes ranging from the sand through gravel to cobble size fractions. The mean valley slope is 1.2%. The river is typical of braided rivers found in outwash plains in front of both glaciers and ice sheet outlets. Field-measured maximum water depths varied from ca. 0.20 m in secondary channels to more than 0.60 m in main channels.

Applying empirical estimations for the attenuation coefficient based on water column turbidity, the lowest measured turbidity of ca. 250 NTU produce maximum extinction depths of around 0.30 to 0.50 m (Rose et al., 2014). At these depths, there is very little texture available on the bed and the form of the exponential absorption of light with depth means very poor precision in depth estimates. This is why both two-media photogrammetric correction and image-based approaches are not suitable for this kind of stream.

FIGURE 1 Location of the study area, streamflow hydrograph and spatial configuration of the glacier d'Otemma proglacial forefield (45° .56'03.544"N, 7°24'42.197"E) from a both aerial and ground-level perspective. Red dots on the flow hydrograph (a) show the three days of the survey (Table S1.1. in Supplementary Information S1). Coloured dots in the forefield maps (b) refer to measured cross-section water depths used for the calibration (orange) and for the validation (blue) process. Water stage data for the 2020 melt season are available in Müller & Miesen (2022).



In this study, we used field-data collected on the 18th of August 2020 and on the 8th and 10th of September 2020. These have different measured water depth ranges because of the different melt rates and discharge rates (Q_w) experienced by the glacier during the melt season (Figure 1): mean Q_w during the data acquisition was $5.29 \text{ m}^3/\text{s}$ on the 18th of August, $2.98 \text{ m}^3/\text{s}$ on the 8th and $3.11 \text{ m}^3/\text{s}$ on the 10th of September. We describe data collection below.

2.2 | Methodology

Figure 2 gives an overview of the methodology developed to estimate spatially-continuous water depths using morphometric parameters using: (1) orthomosaics of the alluvial plain; and (2) the related Digital Elevation Models (DEMs). These parameters are combined with geo-referenced point measurements of water depth from within the inundated zones obtained using a differential GPS (dGPS) survey to develop statistical models for channel bathymetry. In this study, we

focus on analyses conducted around daily low discharge conditions (Figure 1) with the ultimate aim of producing daily DEMs for morphological change detection.

The bathymetric model is written in MATLAB (version 2019a) and freely available in Mancini et al. (2024).¹ The SfM-MVS-derived orthomosaic is used to classify the study area into wet and dry regions. Following Westaway et al. (2003), the resulting classification is used with the associated DEM to extract elevations along the wet-dry interface. These are interpolated to create a flat water surface map which can be combined with texture-estimated water depths to obtain topographic data in inundated zones (Westaway et al., 2003). The field-collected water depth measurements are used to develop both single date-specific and pooled statistical models. These models are constructed from a series of heuristic statements that define which morphometric parameters we derive to model measured water

¹The code will be made available if the paper is accepted for publication.

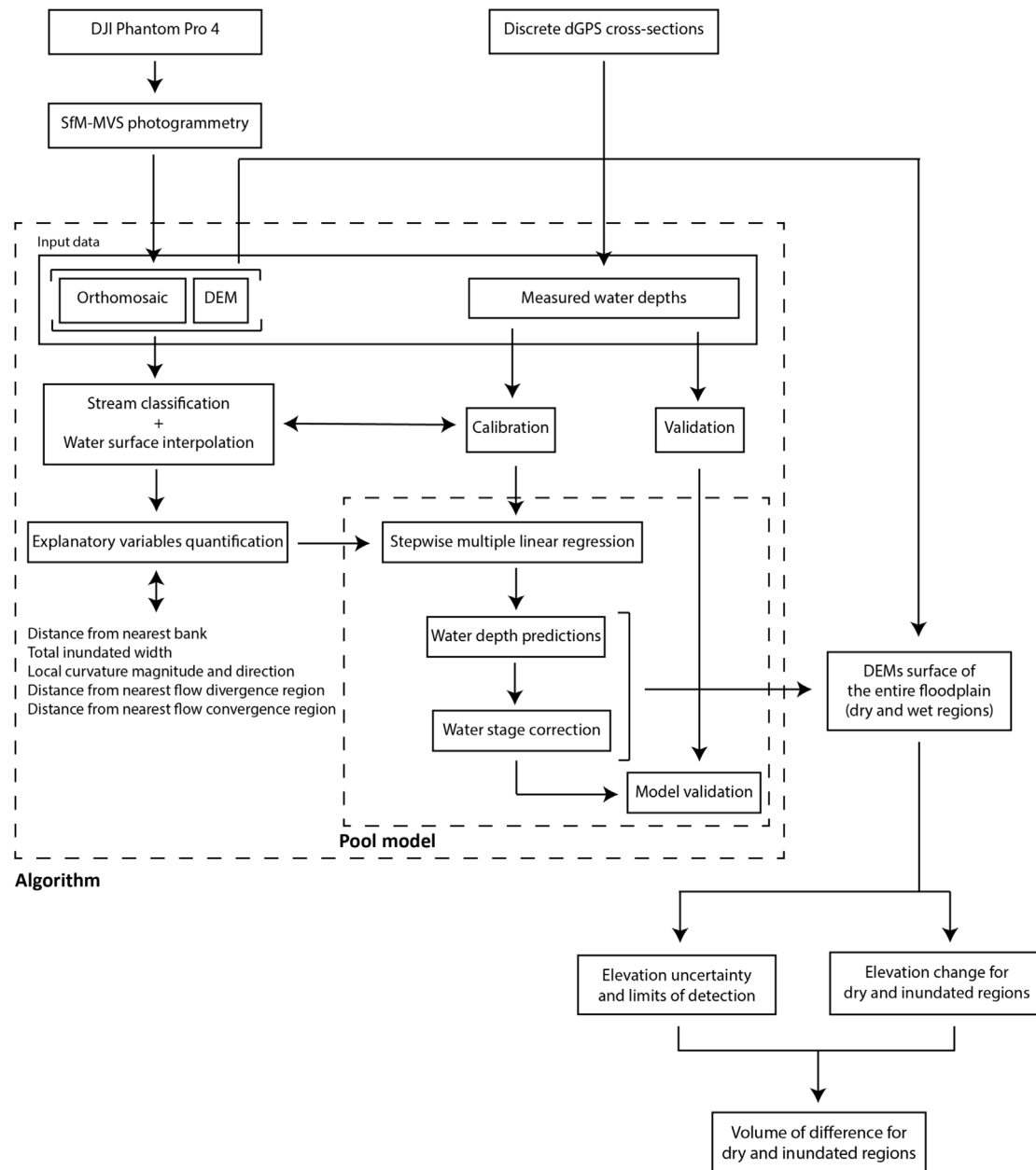


FIGURE 2 Schematic overview of the used methodology.

depths. We justify the choice of these statements and explain their quantification below (Section 2.3.4).

For each field-collected dataset, a subset of depths is used in a stepwise linear regression to identify which of these parameters make a statistically significant contribution to water depth variation in space, and so to define the form of the final multiple regression model. The models are then applied to data points not used in calibration to validate them. The final models are applied to the full braidplain to provide spatially-continuous water depth maps at the proglacial-margin scale. The number of depths that can be measured is limited by the constraint that the stage should not change significantly during data collection leading to relatively small sample sizes. Thus, we also tested the effect of merging the three 2020 datasets to increase sample size. Resulting water depth distributions for inundated zones are combined with SfM-MVS photogrammetric data for dry zones to create DEMs of the entire floodplain. Following Lane et al. (2003) we produce spatially-varying estimates of uncertainty

and levels of detection, and then volumetric changes estimates in both dry and inundated regions. We would expect the quality of elevations in inundated zones to be degraded as compared with the dry zones and this last step allows us to assess whether or not this method is fit for the purpose of morphological change detection and volume estimation in an actively braiding glacier-fed stream.

2.3 | Methods

2.3.1 | UAV data acquisition and SfM-MVS photogrammetric processing

Drone imagery was acquired using a DJI Phantom 4 Pro UAV in the early morning on each of the three survey dates when the floodplain experienced low flow and relatively stable conditions (Supplementary material S1; Roncoroni et al., 2022). The drone was

mounted with a FC6310 camera containing a 1-in. CMOS sensor has a focal length of 8.8 mm and a pixel pitch of 0.24 mm, so producing $5'472 \times 3'648$ pixel images. Flight plans were designed in Pix4DCapture (version 4.8), with an overlap of 80%. The survey strategy followed James et al. (2020) in order to optimize the photogrammetric process and to reduce the magnitude of systematic error in derived DEMs. The study area was divided into four zones, each one surveyed with two orthogonal grid missions having a camera angle at nadir (90° at 80 m height) and with two additional circular missions at 60 m height where the camera was self-oriented towards the centre of the scene (Roncoroni et al., 2022). The theoretical ground sampling distance per flight varied between 0.6 and 0.8 cm/pixel depending on camera height and obliquity. Each survey started at 8 am and took ca. 3.5 hours to cover the entire proglacial outwash plain extent shown in Figure 1. This was undertaken daily throughout the melt season.

We installed 77 ground control points and collected 170 independent checkpoints to evaluate model quality. These were measured using rapid static GNSS-RTK surveys set at 2 minutes per point using a dGPS Trimble R10, with a known base station (corrected using the fixed monitoring Swiss Federal Office for Topography provided system via SwiPos©; Mancini & Lane, 2020). Data points were corrected to the Swiss CH1903+/LV95 coordinate system. Point precisions were comprised between ± 0.02 m and ± 0.04 m in the horizontal and vertical, respectively.

For each day of the survey, the post-processing of the imagery was performed using the SfM-MVS photogrammetric software Agisoft Metashape (version 1.5.5), following steps detailed in James, Robson, d'Oleire-Oltmanns, and Niethammer (2017), James et al. (2020), and James, Robson, and Smith (2017). First, images that were blurred and/or too contrasted, that had few (~ 500) and/or an uneven distribution of tie points and/or that presented large tie point residuals (> 1 pixel), were discarded (James et al., 2020). Second, images were aligned and tie points were automatically extracted from matching images. At this stage, tie points that were observed in only a few images (< 3) were discarded (James et al., 2020). Third, we used a statistical method (James et al., 2020; James, Robson, d'Oleire-Oltmanns, & Niethammer, 2017), implemented in Agisoft Metashape as an external plugin to improve the SfM-MVS bundle adjustment. It uses Monte Carlo simulation: (a) to identify the camera model that minimizes systematic error; and (b) to investigate the impact of individual GCPs on overall model quality. This process is fully described in Roncoroni et al. (2022) for the datasets used here. The procedure resulted in a camera model composed of 5 parameters and 52 GCPs (Supplementary Information S1). Table 1 summarizes the results.

Fourth, aided by the semi-automatic marker identification available in Metashape, GCPs (Supplementary material S1) were introduced to help constrain the bundle adjustment. The RMS errors for

both GCPs and 170 independent checkpoints are shown in Table 1. Finally, point clouds were densified and used to produce orthomosaics and DEMs for each survey at a resolution of 0.05 m and 0.20 m, respectively (Table 1). For the morphometric analysis described below, the orthoimages were resampled to 0.20 m for computational reasons. More details on the methodology are given in Roncoroni et al. (2022). Orthomosaics produced by and used in this study are freely available in Roncoroni, Mancini, and Miesen (2023) and the final DEM products are available in Mancini et al. (2024).

2.3.2 | Sampled point data for model calibration and validation

The Trimble R10 dGPS was also used in rapid-static GNSS-RTK mode to obtain discrete geo-referenced points of the riverbed at the same time as UAV image acquisition. Due to the difficulties in maintaining the rover in a stable position for long periods because of water currents, the sampling time per point was set to 30 seconds. As with the GCPs, data were precise to ± 0.02 m in the horizontal and ± 0.04 m in the vertical component.

For the bathymetric modelling, topographic measurements were collected in the form of cross-sections extending away from selected locations on channel banks. The use of cross-sections was deemed preferable as it made sure that we obtained a good depth range extending from the shallowest (near bank) to the deepest water. Cross-sections were chosen such that we captured a range of different morphological features (e.g. ones with both fewer secondary channels and more secondary channels; some with convergence zones and some with divergence zones; and a range of channel widths). Within cross-sections, we maintained an average point spacing of ca. 0.4 m. Due to safety considerations, data collection in the deepest regions was challenging meaning fewer data could be acquired. The collected cross-sections were then randomly split into two halves for calibration and validation purposes.

2.3.3 | Image processing to obtain a water surface DEM

The SfM-MVS-derived orthomosaics were classified into wet and dry zones. First, we converted the orthomosaic from RGB to grayscale to reduce unwanted noise related to changing light intensity (Gao et al., 2008; Liu et al., 2018). Random pixels falling within inundated regions were manually sampled to define the spectral range of turbid water. These were used to train a simple signature-based classification model in MATLAB to generate a binary raster of wet and dry regions: pixels having a value falling within the spectral range of turbid water

TABLE 1 Evaluation of bundle adjustment performance in terms of GCP error, point cloud quality and DEM vertical difference by comparison with 170 independent checkpoints.

	GCP RMS error [m]	Total number of points in dense cloud	Checkpoints Z mean and standard deviation of error (SDE, in brackets) [m]
18th August 2020	± 0.049	101'154'741	0.009 (± 0.029)
8th September 2020	± 0.014	92'300'262	0.009 (± 0.031)
10th September 2020	± 0.013	93'812'486	0.011 (± 0.028)

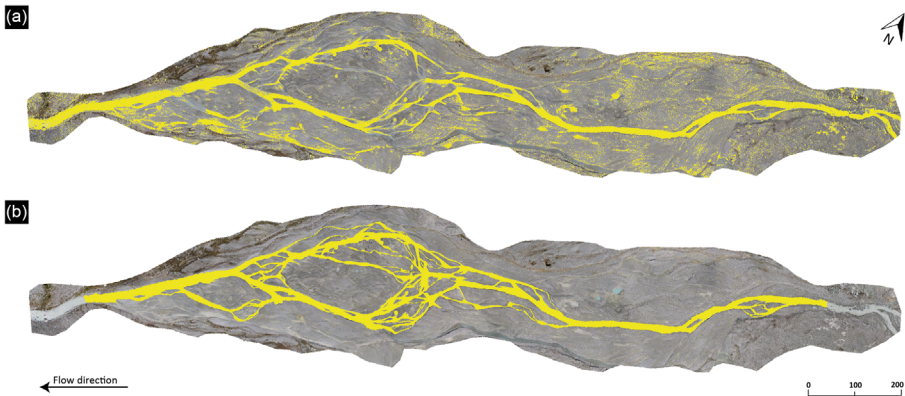


FIGURE 3 Turbid water detection for the 18th of August dataset using (a) the automated spectral signature method and (b) final result after manual correction.

were classified as 1, otherwise as 0. Second, the resulting inundation map was manually corrected by comparing it visually with the respective orthomosaic (Figure 3; Roncoroni, Mancini, Miesen, Müller, et al., 2023). Points in the dry-wet boundaries were identified and used to extract coordinate triplets from the DEMs obtained using the SfM-MVS photogrammetry. These were then interpolated using Delaunay triangulation in order to produce a flat water surface within each DEM for representing sub-critical flow conditions (Westaway et al., 2003).

2.3.4 | Morphometric parameters

Given that the focus is a braided river, we developed five heuristic statements that were then quantified to drive the statistical model for estimating water depth: (1) the depth of a river increases with distance from the nearest bank (this follows from within cross-section application of the principle of maximum entropy; Farina et al., 2015); (2) where the total inundated width of all channels in a braidplain cross-section is higher, flow velocities and hence erosion depths should be lower, assuming steady discharge (Mosley, 1983); (3) channel curvature redistributes momentum laterally and so causes the deepest zone to migrate towards the outer bank of the channel (Ashmore, 1982; Begin, 1981); (4) flow divergence leads to deposition and hence lower flow depths, while (5) flow convergence leads to scour and hence higher flow depths (Ashworth, 1996; Lisle et al., 1991). Their computation is described below and their spatial distribution is shown in [Supplementary Information S2](#).

Distance from the nearest bank

In rivers, channel width, depth and velocity respond to water discharge via modification of topographic (e.g. via scour or via bank erosion) or hydraulic (roughness, bed slope) parameters (Leopold & Maddock, 1953; Mackin, 1948; Mosley, 1983). If discharge increases, within a cross-section, the river may become wider, deeper or faster (Leopold & Maddock, 1953). The increase in depth may result from either rising water level or (vertical) riverbed erosion; the increase in width is achieved through (lateral) bank erosion. Vertical and lateral erosion are not independent as where vertical erosion occurs close to a river bank there is a greater probability that the river bank will be over-steepened and, especially where the river bank is not cohesive, it will fail. It might then be stated that water depths are likely to be greater farther from a river bank. Thus we estimated the distance

from the nearest bank by applying an Euclidean distance operator to the wet-dry image; this measures the shortest distance for each wet pixel to the river bank.

Total inundated width

The relation between discharge and morphologic modification is complex in a braided river as in addition to the river becoming wider and deeper as discharge rises there is also an increase in the number of channels. This reduces hydraulic efficiency and hence vertical erosion as compared to a single-thread channel. Thus, we would expect river channel bathymetry also to reflect the total inundated width, with lower total widths likely to be faster and deeper.

Estimating total inundated width is not evident in a river with continuously converging and diverging channels across a number of different scales. The solution adopted here involves a two-step approach (Figure 4). First, we estimate the width of the local channel, here expressed as twice the Euclidean distance between the nearest dry point on the river bank (b) and the channel centerline (c) at each cell (i) in the inundated zone ($2d_{bc}^i$). The channel centerline is mapped using a skeletonization algorithm. This does not give the true “hydraulic” centre-line as the analysis is done on a surface map of inundated area rather than distributions of flow velocity and water depth, but comparisons with a manually digitized centre-line suggested an excellent level of agreement. Second, we add other non-local channel widths ($2d_{bc}^k$) falling on an imaginary orthogonal line to the considered cell i to get the total inundated width.

To obtain the total inundated width for each local channel i , we use a morphological structuring element (STREL) to identify which non-local channel widths k apply to each i (Figure 4). The STREL is a square matrix oriented so the diagonal is perpendicular to the local channel cell i with an angle given by the direction of local curvature (see below). The diagonal is set to be twice as long as the braidplain width, in our case 1,400 cells. Any other intersection of the STREL diagonal with a centre-line (excluding the local centerline) indicates a non-local channel (k) of width $2d_{bc}^k$ contributing to the total inundation width for i . The total inundation width (Tiw) is then computed as:

$$Tiw = \sum_{k=1}^n 2d_{bc}^k + 2d_{bc}^i \quad (\text{Eq1})$$

Where:

Tiw = total inundation width;

$2d_{bc}^i$ = width of the local channel

FIGURE 4 Illustration of the approach to total inundation width estimation using morphological structuring elements (STREL, red square). In this example, the local channel width ($2d_{bc}^i$, orange arrow) is combined with two non-local channel widths ($2d_{bc}^k$, blue arrows) to give the total width for that specific cell. Transects illustrate the topographic effects of secondary circulations in curved channels (A) and in flow divergence (B) and convergence regions (C). Plus and minus refer to deposition and erosion, respectively.

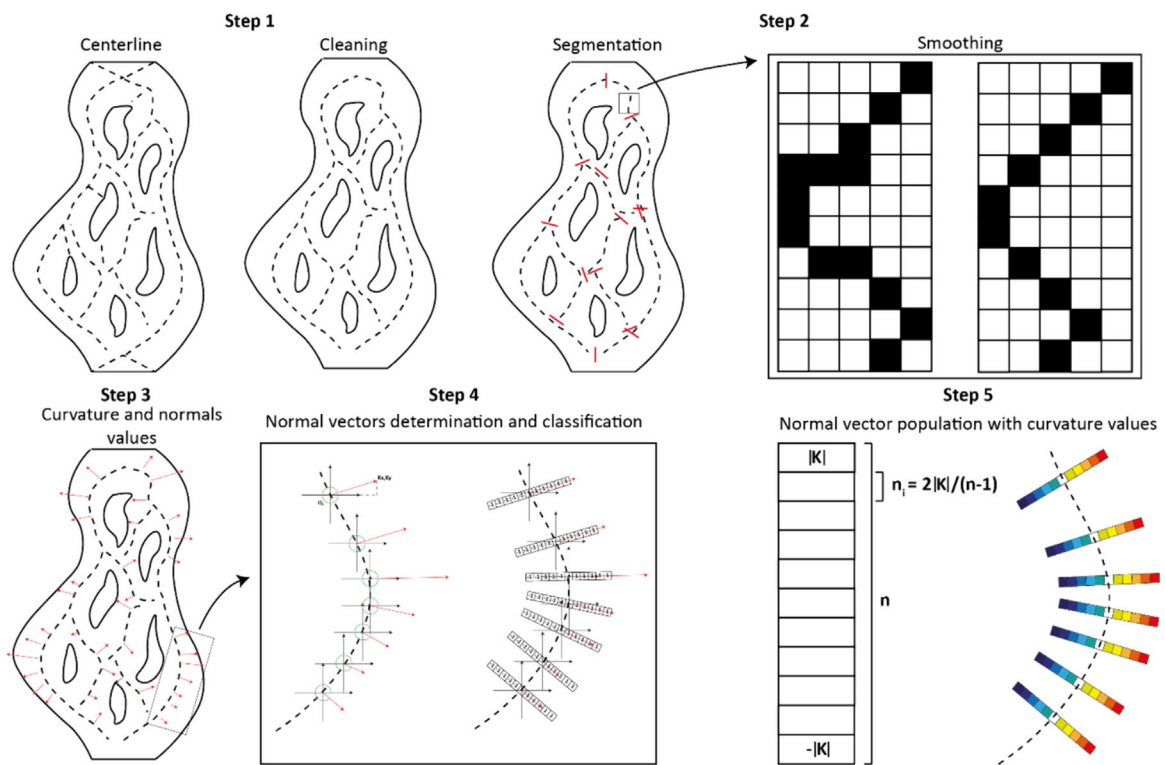
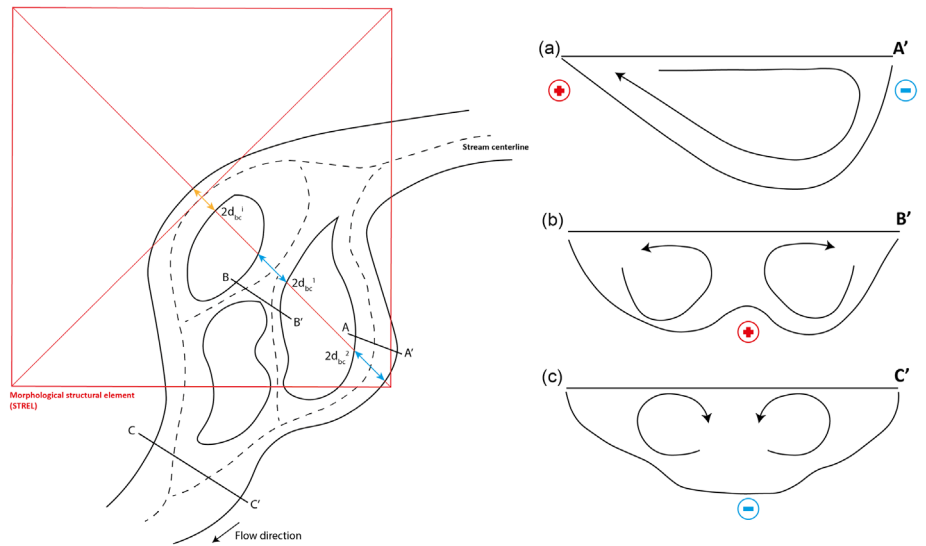


FIGURE 5 Methodological approach used to quantify the local curvature magnitude and direction variable. Step 1: centerline cleaning from noisy segments; step 2: segmentation of the cleaned centerline in multiple transects to apply a smoothing function needed to avoid abrupt direction changes having a potential effect on real curvature values; step 3: determination of normal vector coordinates and magnitudes; step 4: determination of normal vector angle in reference to the first quadrant; step 5: classification of pixels of regions of negative (blue gradient) and positive (red gradient) curvature regarding the local magnitude and normal vector direction.

$2d_{bc}^k$ = non-local channel widths;
 n = number of diagonal intersections.

Local curvature magnitude and direction

The local curvature magnitude and direction are based on determining streamlines (or centerlines in terms of the digitized inundated area). As shown in studies of river meandering (e.g. Brice, 1975) and braiding (e.g. Ashworth, 1996; Richardson & Thorne, 1988), curvature is a key driver of fluvial morphodynamics because it leads to secondary

circulation; it has been measured in proglacial rivers (Ashmore, 1982; Ashmore et al., 1992). Rivers flowing on flat and poorly-vegetated floodplains are likely to be shaped by this secondary flow, which has the effect of shifting erosion towards the outer bank and deposition towards the inner bank (Figure 4). This results in a transverse displacement of regions having higher and lower water depths within the channel cross-section (Ashmore, 1982; Powell, 1998). Thus, local curvature magnitude and direction can be used as a proxy to determine the spatial distribution of secondary flow (e.g. Frascati &

Lanzoni, 2009, 2013; Parker et al., 2011) and its effects on water depths.

The local curvature magnitude and direction calculation (Figure 5) start with the centerlines used in the estimation of total inundation width. First, a manual reworking of the centre-line is needed to remove unwanted segments coming from abrupt and sudden changes in the shape of the digitized polygon. Second, segmentation is used to create individual centre-line segments in individual reaches limited in their upstream and downstream direction by flow divergence and convergence units, respectively). These segments are subsequently smoothed using a loess filter to reduce noise in the data (Tate et al., 2005). Third, the curvature is calculated following Mjaavatten (2020). This latter returns, for each cell composing a centerline segment the local curvature values and the coordinates (k_{xi}, k_{yi}) describing the direction of orthogonal vectors for each point composing the segment. These outputs were used in the fourth step to differentiate the stream into regions of positive curvature, which would displace momentum and hence depth away from the centre-line and regions of negative curvature with the opposite tendency (Figure 4). This is done for every point composing each segment by assigning them a diagonal matrix of specific length and angle. The length simply corresponds to the local channel width, while the angle is given by the difference between the direction of orthogonal vector in a local streamline cell (k_{xi}, k_{yi}) and the x-axis of an imaginary Cartesian plan calculated in a counter-clockwise direction; cells located on the half having the same orientation of the normal and hence in the direction of positive curvature were assigned a value of +1; those in the opposite orientation have -1. Finally, the magnitude of the curvature is calculated by attributing at the outermost diagonal cells the curvature magnitude found by applying Pythagoras' theorem to the previously determined normal vector components:

$$|K_{ji}| = \sqrt{k_{xi}^2 + k_{yi}^2} \quad (\text{Eq2})$$

Where:

$|K_{ji}|$ = magnitude, or length, of the normal vector j at point i of the centreline;

k_{xi} = coordinate X of the normal vector having origin in i ;

k_{yi} = coordinate Y of the normal vector having origin in i .

As the total number of cells composing the normal vectors is known, we then fill cells in the rest of the diagonal by calculating a decreasing interval from the maximum magnitude value (+K) or an increasing interval from the minimum magnitude value (-K). This procedure is defined by:

$$n_{ji} = |K_i| - \sum_{n=1}^{n-1} 2|K_i|/(n-1) \quad (\text{Eq3})$$

Where:

n_{ji} = curvature magnitude value at the cell i of the normal vector j ;

$|K_i|$ = magnitude/length of the normal vector at point i of the centreline;

n = total number of cells composing the vector j .

An interpolation (Delaunay triangulation) is then applied to fill points not falling in one of the diagonals in order to have a continuous matrix of curvature values.

Planform streamline convergence and divergence

Streamline convergence and divergence locations related to bars in braided rivers can also influence erosion and deposition and hence water depth distributions. This is reflected in studies of deposition at bifurcations and on bar-heads (Best & Reid, 1984; Best, 1988; Ashworth, 1996; Figure 4), and erosion at confluences (Bristow & Best, 1993; Ashworth, 1996; Figure 4).

Flow convergence and divergence regions were visually identified based on the inundation map. The distance from each inundated cell to the nearest flow convergence and divergence region is then automatically computed in a procedure involving three steps. First, for each convergence and divergence region, a null matrix having the same dimensions of the entire study area is generated, and the value 1 is attributed to their exact spatial location. Second, radial distances are computed. Third, for each cell composing the inundated area, the closest divergence and convergence regions were found by using the distance matrices as a lookup table.

Measured water depth

The surveyed water depth is the response variable of the model. The dGPS points give elevations which need to be combined with the water surface to give water depths. This is done by calculating the Euclidean distance between the 2D coordinates of each sampled dGPS topographic point and all the cells composing the triangulated water surface. The minimum calculated distance is kept, as the orthogonal and shorter distance between the riverbed and the water surface.

2.3.5 | Water depth prediction: model calibration, application and validation

Before modelling water depths, we checked the basic assumptions required in multivariate regression analysis, notably regarding multicollinearity between independent variables (Olsen et al., 2020). The degree of collinearity between variable pairs was computed using the variance inflation factor (VIF) (e.g. Neter et al., 1983; Thompson et al., 2017). A VIF value > 10 indicates that two variables were highly correlated with each other and could lead to multicollinearity if they were both included within a model.

Model calibration was based upon a step-by-step multiple linear regression (Breux, 1967; James et al., 2013; Maxwell, 1975; Olsen et al., 2020) aimed at explaining the measured water depth from the set of morphometric variables):

$$y = b_0 + b_1x_1 + \dots + b_i x_i + e \quad (\text{Eq4})$$

Where:

y = response variable (i.e. measured water depth);

x_i = observations associated to the independent variable i ;

b_0 = y-intercept;

b_i = partial regression coefficients (weights) associated to x_i ;

TABLE 2 Characteristics of the dGPS surveys in terms of total number of points and stream cross-sections for both calibration and validation sub-samples associated with each dataset (Figure 1). In square brackets the percentage of the number of points compared to the total number of points composing the dataset.

Date	Total		Calibration		Validation	
	Number of points	Cross-sections	Number of points	Cross-sections	Number of points	Cross-sections
18th August 2020	206	23	112 [54.4%]	12	94 [46.4%]	11
8th September 2020	259	37	136 [52.5%]	21	123 [47.5%]	20
10th September 2020	157	25	82 [52.2%]	18	75 [47.8%]	17

e = residuals (i.e. variance not explained by the model).

Variables were added iteratively starting with the most important, in terms of percentage of explained variance, until no further variables resulted in a statistically significant ($p < 0.05$) increase in explanation (Draper & Smith, 1998).

Stepwise regression was applied to the three datasets individually (Figure 1 and Table 2). The resultant models were then applied to the entire study area to determine predicted water depths in all flooded cells for each calibration date. To account for the difference in discharge rates over the 3.5 hours of UAV survey (2.55 m³/s to 8.04 m³/s [+315.33%] on the 18th of August, 1.81 m³/s to 4.16 m³/s [+231.33%] on the 8th and 2.24 m³/s to 3.99 m³/s [+177.89%] on the 9th of September; Figure 1), the results were corrected for the effects of changing water stage conditions. The associated methodology is fully presented in Supplementary Information S3.

The model was evaluated quantitatively in two ways. First, the residual errors of the fitted model and their spatial distribution were considered. Second, local predicted water depths were compared to independent measurements (validation dataset, Table 2) and differences between measured and predicted depths were quantified (R^2 and standard deviation of error).

2.3.6 | Pooling of calibration data

As the number of datapoints available for each dataset was limited, a model calibrated with all available water depth measurements was developed (Figure 1 and Table 2). The aim was to obtain more statistically significant results that could be applied to dates where no calibration data were available. The resulting relation was then applied individually to the three field-collected datasets to produce water depth prediction maps, and validated using the three sets of independent measurements (validation datasets, Figure 1 and Table 2).

2.3.7 | Elevation estimation, elevation uncertainties, limits of detections and volumetric change estimates

Water depths were converted into wet-bed elevations following Westaway et al. (2003) by subtracting the predicted water depths from the interpolated water surface in the DEM. Elevation uncertainties were determined as the sum in quadrature of the uncertainties related to both water depth prediction and water surface in each single DEM (Lane et al., 2003):

$$EU_{ij} = \pm \sqrt{\sigma d_{ij}^2 + \sigma e_{ij}^2} \quad (\text{Eq5})$$

Where:

EU_{ij} = elevation uncertainty in cell (i,j);

σd_{ij} = standard deviation of water prediction error in cell (i,j) derived from prediction uncertainty bounds from the water depth modelling;

σe_{ij} = standard deviation of water surface error in cell (i,j), taken as the dry DEM uncertainty.

For dry cells, Equation 5 is modified as $EU_{ij} = \sigma e_{ij}$. The standard deviation of error for dry regions (the dry DEM uncertainty in Equation 5) was determined by comparing the 170 field-measured and photogrammetrically reconstructed elevations of stable areas. Equation 5 gives a spatially explicit estimation of DEM uncertainty for both dry and wet cells.

DEM_s of difference (DoD) were determined by subtracting the oldest DEM from the most recent one (i.e. DEM_{t2}-DEM_{t1}) and filtered according to the spatial distribution of the limits of detection (LoD) set at 68% (Brasington et al., 2003; Lane et al., 2003) using:

$$LoD_{ij} = \pm t \sqrt{(EU_{ij}^t)^2 + (EU_{ij}^t)^2} \quad (\text{Eq6})$$

Where:

LoD_{ij} = limit of detection in cell (i,j) [m];

t = Student's confidence interval threshold (1 at 68%).

EU_{ij}^t = Elevation uncertainties in cell (i,j) at times t .

DEM_s of difference were filtered according to LoD maps to highlight only statistically significant geomorphic changes. These were then classified into regions as inundated, dry and transient (i.e. inundated to dry or dry to inundated) between surveys. Finally, volumetric change maps were produced from spatially filtered DoD maps and total volumetric change estimates were computed following Lane et al. (2003) as:

$$V = d^2 \sqrt{n} \sum DoD \quad (\text{Eq7})$$

where:

V = Volume [m³];

d = cell size (i.e. 0.20) [m];

n = number of raster cells in DoD;

DoD = DEM_{t2}-DEM_{t1} spatially filtered by LoDs (Equation 6).

TABLE 3 Stepwise regression outputs. Variable considered into multiple linear regression and predictor relative weights obtained at each step. P-values show that the selected variables composing the multiple linear regressions are statistically significant, while both R-squared and standard deviation of error (SDE) behaviour highlight the effect of a new variable on the overall model prediction capacity.

Date	Step	Variable	Coefficient b				Statistics		
			b ₀	b ₁	b ₂	b ₃	R ²	SDE	p-value
18th August	1	Dist. nearest bank	0.190	0.093			0.375	0.138	2.2×10^{-9}
	2	Divergence	0.144	0.069	0.004		0.545	0.118	4.7×10^{-9}
8th September	1	Total Width	0.371	-0.012			0.367	0.081	7.3×10^{-7}
	2	Dist. nearest bank	0.305	-0.010	0.033		0.450	0.075	7.2×10^{-4}
	3	Convergence	0.261	-0.008	0.026	8.8×10^{-4}	0.489	0.072	0.002
10th September	1	Dist. nearest bank	0.148	0.076			0.434	0.088	1.3×10^{-11}
	2	Divergence	0.134	0.064	0.001		0.537	0.079	2.3×10^{-6}
	3	Convergence	0.138	0.069	0.003	-0.003	0.610	0.073	2.6×10^{-4}

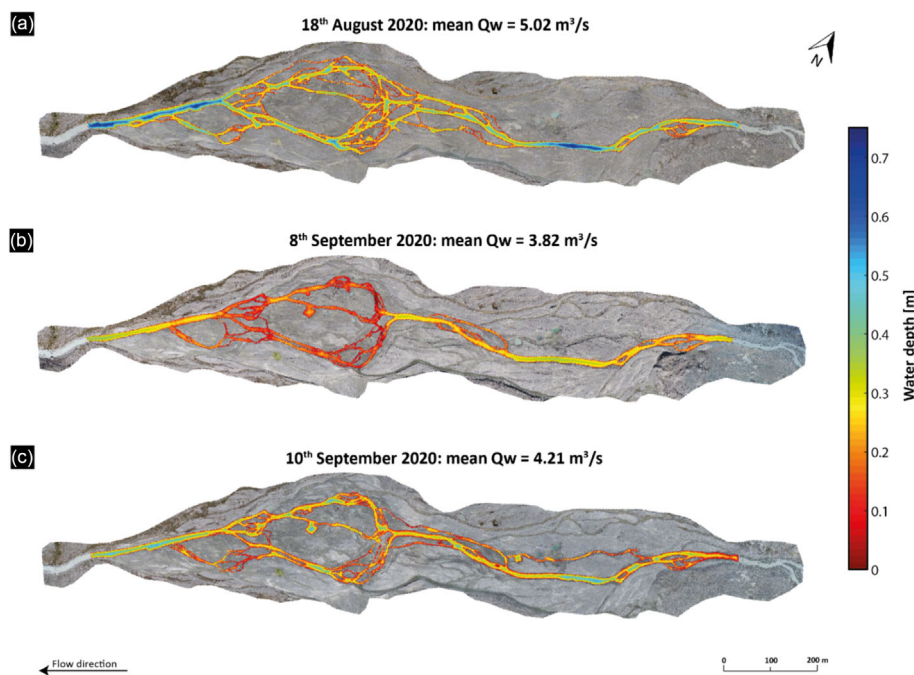


FIGURE 6 Predicted water depth corrected by the changing water stage occurred along the UAV surveys. Mean discharge rates during both UAV-survey and water depth acquisitions are: 5.29 m³/s on the 18th of August, 2.98 m³/s on the 8th of September and 3.11 m³/s on the 10th of September (Figure 1).

The associated uncertainties in volume estimates ($\sigma_{v_{ij}}$) were derived as (Lane et al., 2003):

$$\sigma_{v_{ij}} = \pm \left(\sum_{i=1}^I \sum_{j=1}^J \left[d_{ij}^2 (EU_{1ij}^2 + EU_{2ij}^2)^{0.5} \right]^2 \right)^{0.5} \quad (\text{Eq8})$$

3 | RESULTS

3.1 | Individual predictive models

No pairs of variables were associated with significant collinearity and so none needed to be excluded from the stepwise regression model (Supplementary Information S4). Table 3 shows for each dataset the most significant variables retained, their partial regression coefficient values (or weights) from the multiple linear regressions and the statistics comparing the observed and the predicted water depth values.

Differences in the retained variables and their coefficients were found between dates although all of them include distance from the nearest stream bank. The model describing water depth distribution for the 18th of August 2020 has only two predictors (i.e. distance from the nearest bank and distance from the nearest divergence region), while the 8th of August and the 10th September 2020 datasets identified three. Levels of explained variance (R^2) for the final models are relatively high but differ between dates, and the standard deviations of error are between ± 0.07 and ± 0.12 m. These are degraded as compared with the precision of the dGPS instrument when used in this setting (between ± 0.02 m and ± 0.04 m).

The results of the application of the prediction model for each date (Table 3) are shown in Figure 6 after correction for changing the stage between the start and the end time of UAV surveys (Supplementary Information S3).

Water depth predictions (Figure 6) are higher in regions characterized by a straight fluvial configuration, notably in the most upstream and downstream parts of the study area. In contrast, predictions are more variable and shallower in the braided sectors, although

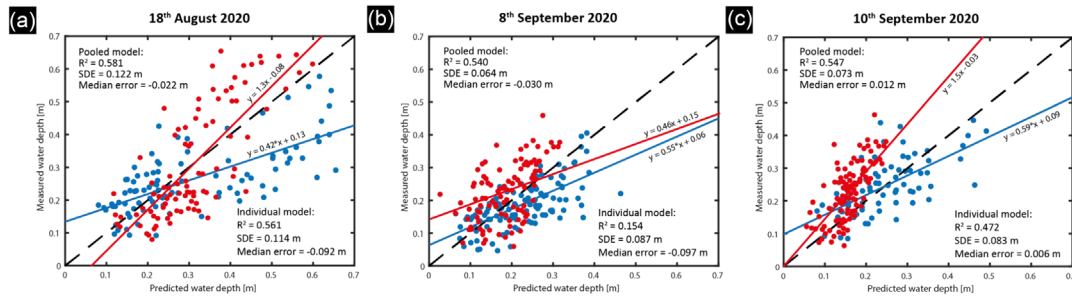


FIGURE 7 Validation plots comparing the predicted and the measured water depths observed in the location shown in Figure 1 for individual (red) and pooled (blue) models.

increasing depths are recorded in regions coinciding with flow confluence regions.

Using the validation datasets, we evaluated the predictive capacity of the multiple linear regression models (Figure 1, Table 2 and Figure 7). The comparison against independent measurements shows that, as implicit in differing statistical success in the calibration results (Table 3), models have different predictive performances.

The 18th of August and the 10th of September validation datasets had the highest R^2 values of respectively 0.561 and 0.472 (Figure 7a and 7c). However, they both tend to over-estimate the measured water depths in shallower regions (up to ca. 0.27 m and ca. 0.05 m, respectively) and to under-estimate deeper ones, especially for the 10th of September. The residual errors for the latter have a wider range (Figure 8a). The model for the 8th September is the one with the lowest R^2 (0.154, Figure 7b) and has an opposite relation compared to that described for the other two datasets with under-estimation for shallower regions (up to ca. 0.27 m) and over-estimation for deeper ones.

Figure 8 shows the residual errors associated with validation points (Figure 1 and Table 2). On the 8th of September, errors were between ca. -0.25 m and +0.1 m, with some outliers falling outside these limits mostly located in secondary channels in the braided sector. On September 10th, the error range is similar but more symmetrical around zero (ca. -0.18 to +0.18 m) with larger errors mainly located in the main channel. The 18th August dataset has the widest distribution of error compared to the other two datasets with points having differences as low as -0.35 m and as big as +0.13 m: higher errors are generally in the main channel, while in the braided sector, they are generally limited to -0.05 to -0.1 m. These results show that the individual models vary in both their precision and their bias.

3.2 | Pooled model

Given mixed validation results when applying the modelling approach to individual datasets, we developed a single model and applied it individually to the three dates for which validation data are available. The correlation matrix and the VIF values for the merged calibration dataset were not collinear (Supplementary Information S5). Table 4 shows the application of the stepwise regression approach to define the generalized multiple linear regression model.

The most significant explanatory variables retained differ from those found when applied individually (Table 3); distance from the nearest river bank; total inundated width; and distance from the nearest convergence

region. The resultant R^2 of 0.648 suggests a statistically significant relation between the retained predictors and the response variable. The standard deviation of error was ± 0.113 m (Table 4).

The qualitative assessment of water depth distribution is in line with that described above for the individually calibrated models (Figure 9): deeper water in the upstream and downstream parts of the study area where the river is more confined; shallower in the braided sector with more variability in regions affected by flow convergence. Predicted depths are generally higher for the August dataset, confirming that the generalized model is able to discriminate between higher and lower flow conditions (Figures 1 and 9a). However, the comparison between water depth maps issued using individual calibrated and pooled models reveals that for the pooled model, predictions are slightly shallower for the 18th of August dataset, deeper for the 8th of September, while consistent for the 10th of September (Figures 6 and 9).

The validation analyses show that the pooled model produces better results than individual models with the obtained R^2 values between 0.5 and 0.6 for all datasets (Figure 7). Despite this, relations all have a common tendency to slightly under-estimate shallower depths and to over-estimate deeper ones, especially for the 18th of August (Figures 7a and 10a). The better performance of the pooled model is also confirmed by the residual errors, which are smaller compared to the individual models with median errors more generally centred on zero and the error range and the outliers more contained (Figures 8a and 10a). The pooled calibration approach reduces the errors in the downstream end of the floodplain where the channel is straight, but also in secondary channels composing the most braided sector (Supplementary Information S6). Especially for the 18th of August dataset, occasional and significant under-estimations are still found in confined flow regions.

3.3 | Model inter-comparison

Table 5 compares the prediction capacity for both specific and pooled models. The latter appears to improve the relationships between the measured and the predicted water depths increasing all R^2 values, while the residual errors improve for two of the three datasets.

Differences in water depths between the individual and the pooled models primarily impact single-channel zones (Figure 11). In these regions, differences for the 18th of August are between ca. +0.05 m and +0.30 m and for the September dates they are between -0.20 m to -0.05 m. In secondary channels within the more

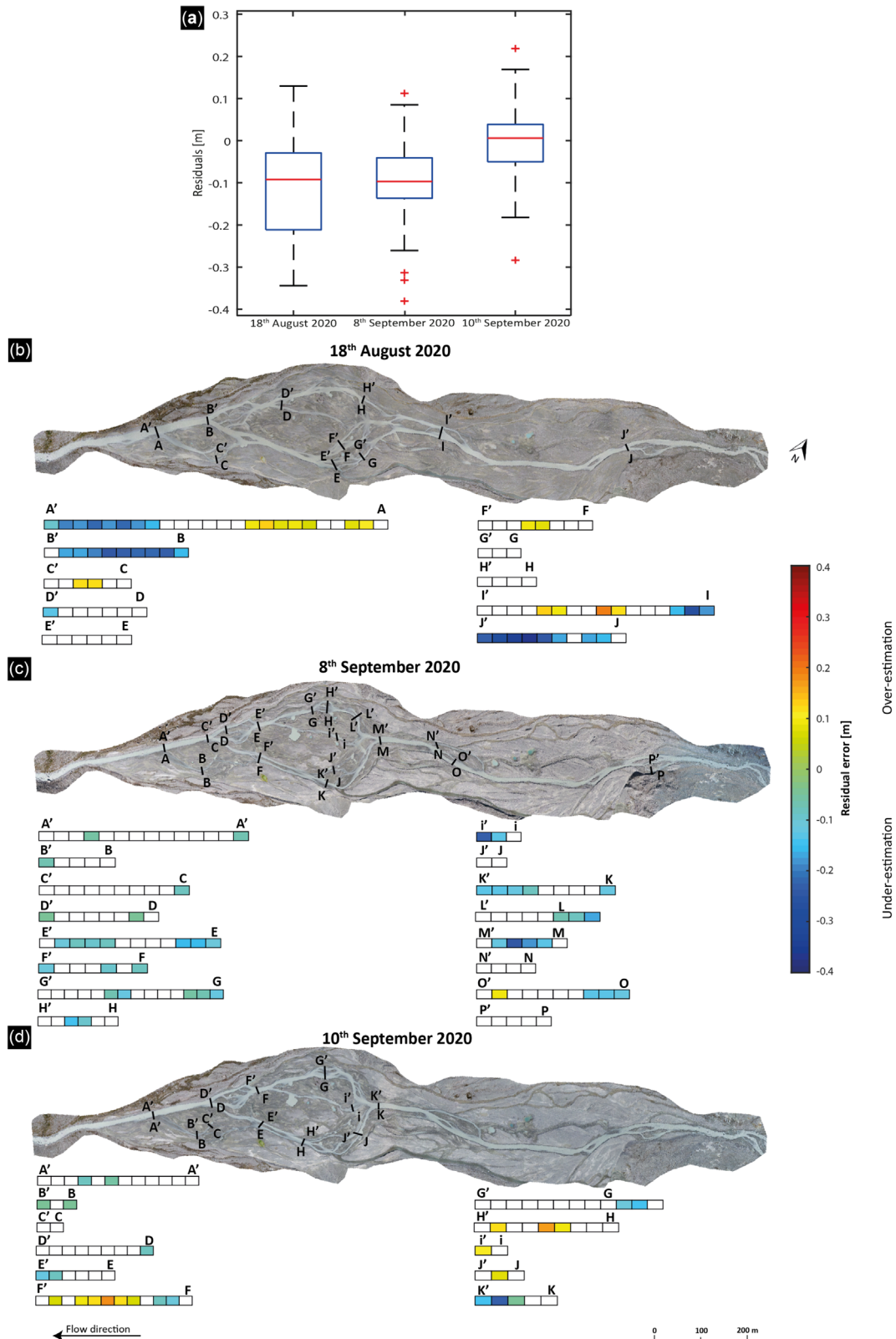


FIGURE 8 Boxplots (a) and spatial distribution of residual errors (b to d) for individual calibrated models. Errors in the interval defined by \pm the standard deviation of the error (SDE, Figure 7) are shown as white. Positive values highlight that the model under-estimate the measured water depth (predictions are shallower than measured data), while negative values refer to over-estimation (predictions are deeper than measured data)

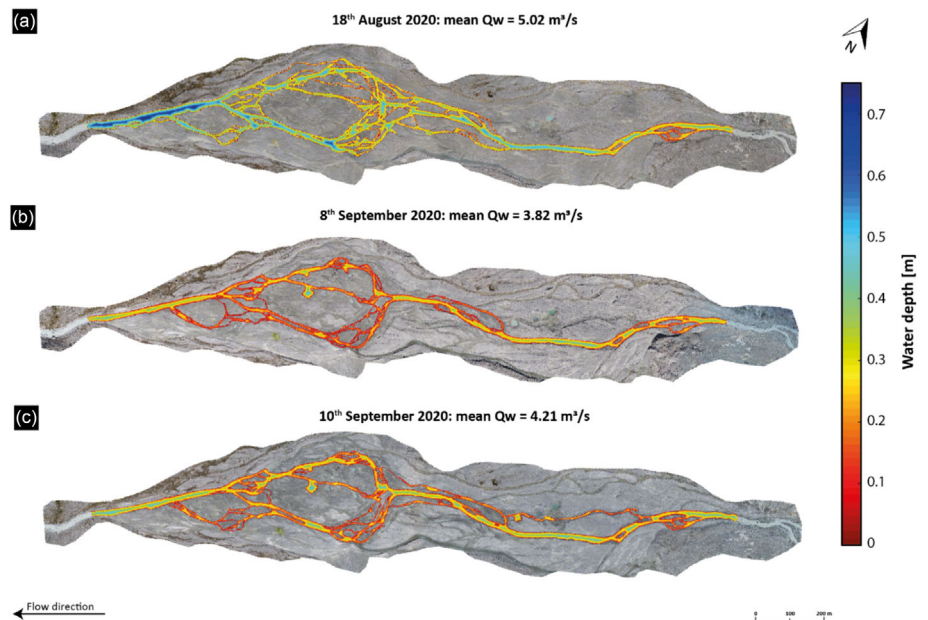
braided section, the differences are smaller, between ca. -0.1 m and +0.1 m in all datasets. Thus, although the pooled model produces more reliable results than the individual model (Table 5), model

performances are more similar for braided zones. In deeper areas, the pooled model performs much better (see [Supplementary Information S6](#) for comparisons).

TABLE 4 Stepwise regression approach applied to the merged 2020 datasets.

Step	Variable	Coefficient b					Statistics			
		b ₀	b ₁	b ₂	b ₃	b ₄	b ₅	R ²	SDE	p-value
1	Dist. nearest bank	0.147	0.083					0.355	0.118	2 × 10 ⁻²⁶
2	+ Total width	0.132	0.073	0.001				0.560	0.115	3 × 10 ⁻¹⁰
3	+ Convergence	0.128	0.076	0.052	0.001			0.648	0.113	8 × 10 ⁻⁸

FIGURE 9 Spatial distribution of water depths issued from the application of the pooled model. Obtained water depths were corrected by the changing water stage that occurred along the UAV surveys. Mean discharge rates during both UAV-survey and water depth acquisitions are: 5.02 m³/s on the 18th of August, 3.82 m³/s on the 8th of September and 4.21 m³/s on the 10th of September (Figure 1)



3.4 | Uncertainty and spatial patterns of levels of detection

The spatial distribution of elevation uncertainty for both dry and wet surfaces was generated for both individual and pooled models following Equation 5 (Figure 12).

Elevation uncertainties are higher for the individual models than for the pooled model. Individual models had elevation uncertainties between ±0.05 m and ±0.12 m for the 18th August, between ±0.035 m and ±0.08 m for the 8th of September and between ±0.04 m and ±0.09 m for the 10th of September dataset (Figure 13a). The pooled model had lower uncertainties of ±0.035 m to ±0.06 m in all datasets. These were not uniform in space, with the braided sector and narrower channels having higher uncertainties compared to single-thread and wider channels (Figure 12).

The spatial distribution of LoDs (Equation 6) is highly variable in space, and higher than when the individual calibrated models were used (Figure 13b). Given that wet areas are more uncertain (Figure 13a), elevation changes in zones permanently inundated were substantially higher. For the individual models, these are ±0.045 m to ±0.14 m for changes between the 18th of August and the 8th of September and between ±0.045 m to ±0.11 m for the period between the 8th September and the 10th September. These are substantially higher than the uncertainties for dry-to-dry elevation changes (±0.042 and ±0.043 m). However, the limits of detection associated with the pooled model are lower, ranging between ±0.045 m and ±0.09 m, and only marginally higher than the mean D₅₀ of 0.06 m. Thus,

implementation of the pooled model reduces elevation uncertainty and improves the detection of morphological change.

3.5 | Volumetric change estimates

Table 6 shows the volume change estimates for regions staying inundated and/or dry within surveys, but also for transient areas (i.e. inundated to dry or dry to inundated). During the investigated period, the proglacial forefield went through net erosion in areas that were both dry (but became inundated at higher discharges) and both inundated on the survey dates presented here. Irrespective of the model used to predict water depth distributions, the vast majority of the erosion took place in inundated regions, or in areas inundated on one of the two dates concerned with contributions to the total volumetric change of up to 69.8%. Transient regions going from wet to dry are associated with deposition (Table 6). Volumetric changes for transient regions (wet-dry or dry-wet) account for more than half of the total volumetric changes at the forefield scale. Dry-only regions, as might be expected, witness relatively less change (up to 15.8% of the total volumetric change). It seems that at the seasonal scale, in this case, significant morphodynamic reorganization was spatially-restricted to specific areas of the proglacial margin. The volume of change estimates from elevation difference maps is slightly higher when the pooled model is considered for determining water depth distribution, confirming observations related to Figure 11.

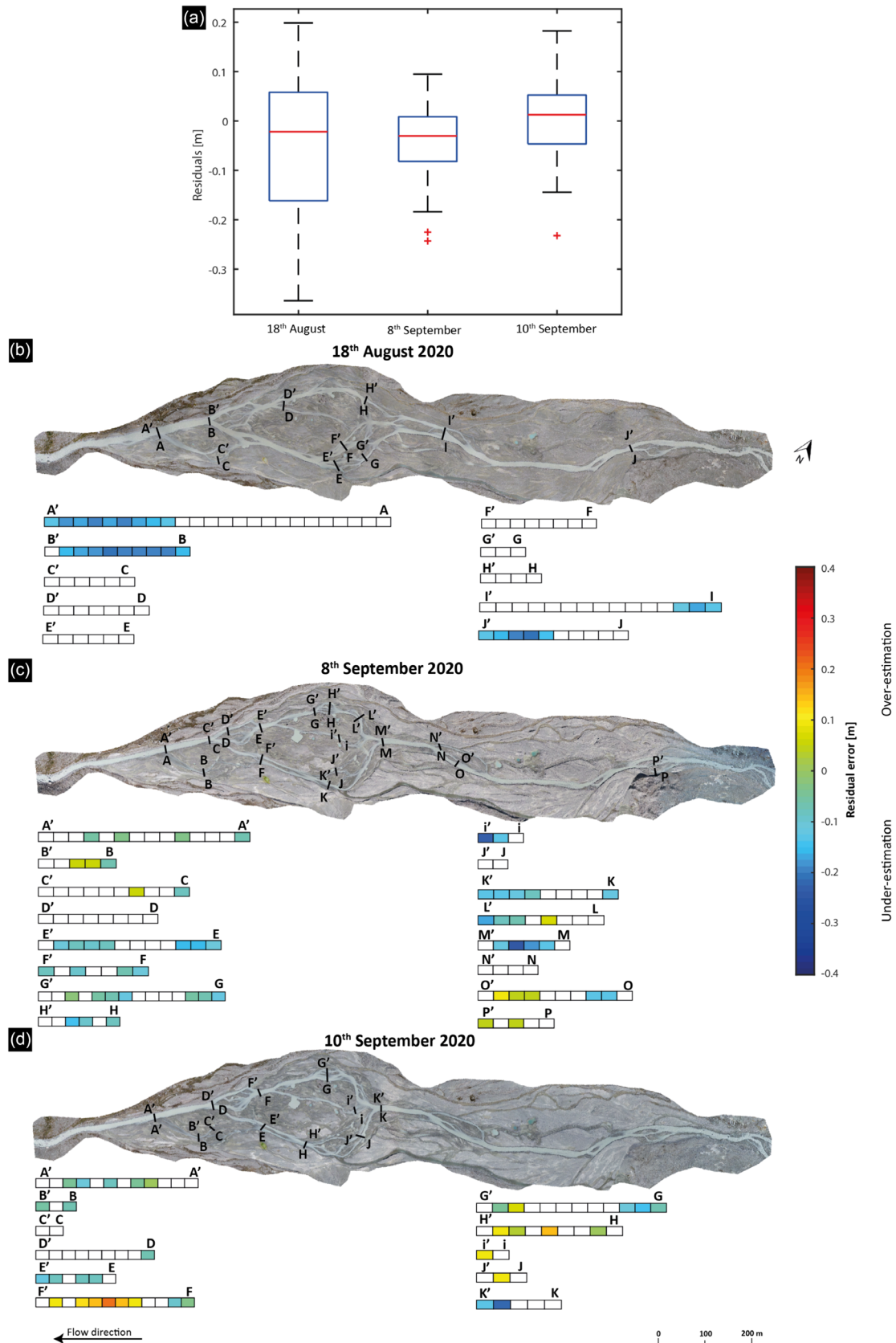


FIGURE 10 Boxplots (a) and spatial distribution of residual errors (b to d) for the pooled model. Errors in the interval defined by \pm the standard deviation of error (SDE, Figure 7) are shown as white. Positive values highlight that the model under-estimate the measured water depth (predictions are shallower than measured data), while negative values refer to over-estimation (predictions are deeper than measured data)

TABLE 5 Comparison between validation R-squared valued and residual error obtained with the application of individually calibrated models and the generalized one.

Date	Statistics	Individual model	Pooled model	% difference
18th August 2020	R ²	0.561	0.581	
	Median [m]	-0.092	-0.022	-70.21
	SDE [m]	0.114	0.122	+12.54
8th September 2020	R ²	0.154	0.540	
	Median [m]	-0.097	-0.030	-68.64
	SDE [m]	0.086	0.064	-25.90
10th September 2020	R ²	0.472	0.547	
	Median [m]	0.006	0.012	-60.32
	SDE [m]	0.083	0.073	-10.84

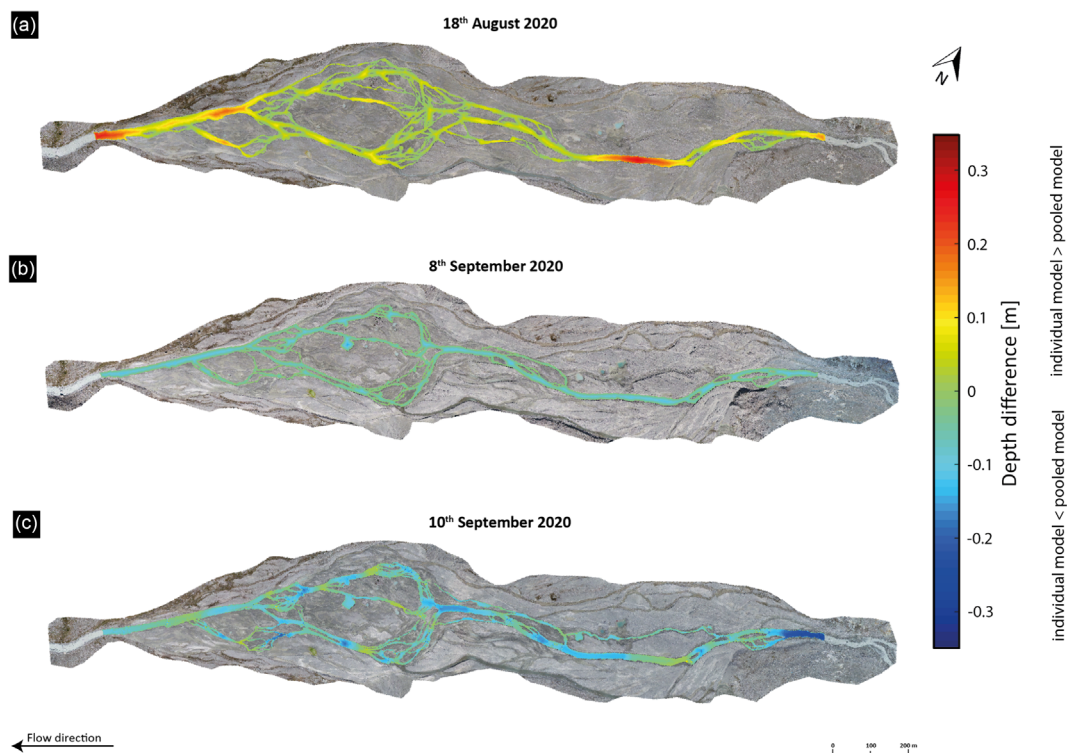


FIGURE 11 Depth of difference maps computed by subtracting predictions issued from the individual models from those given by the pooled one

4 | DISCUSSION

4.1 | Evaluation of specific and pooled models for water depth prediction

The predictive models we develop for water depths in shallow, turbid, glacier-fed braided streams, especially that for the pooled dataset, are encouraging (Table 5). Single calibration models did differ between themselves in terms of predictors and performances (Table 3). The distance from the nearest bank variable was common to all models but three of the remaining four variables (total width, distance from convergence, distance from divergence) did not appear systematically in the models, while curvature did not appear in any of them. These differences between models likely reflect either between-date differences in where and how much data were collected and/or different discharge magnitude at the moment of data acquisition (Figure 1,

Table 2). The extension or the contraction of the proglacial outwash plain due to discharge variation, may have enhanced (or decreased) the importance of certain variables in explaining the measured water depth distributions.

Analysis of R² values (Figure 7) and both magnitude and spatial distribution of standard deviations of error (Figure 8) through the validation process also reveals that models have different predictive capacities. We emphasise that our methodology does not involve the removal of outliers during the calibration process. Braided rivers are complex and non-linear geomorphic systems, with a wide range of water depths (Ashmore, 1988; Phillips, 2003), making it difficult to identify outliers. The resulting predictive capacities for the individual models (Table 3) are more encouraging than their validation results (Figure 7). For instance, the validation relation for the 8th September had a low R² (0.154, Figure 7b) likely because the model struggles to reconstruct the proper bathymetry of braided reaches

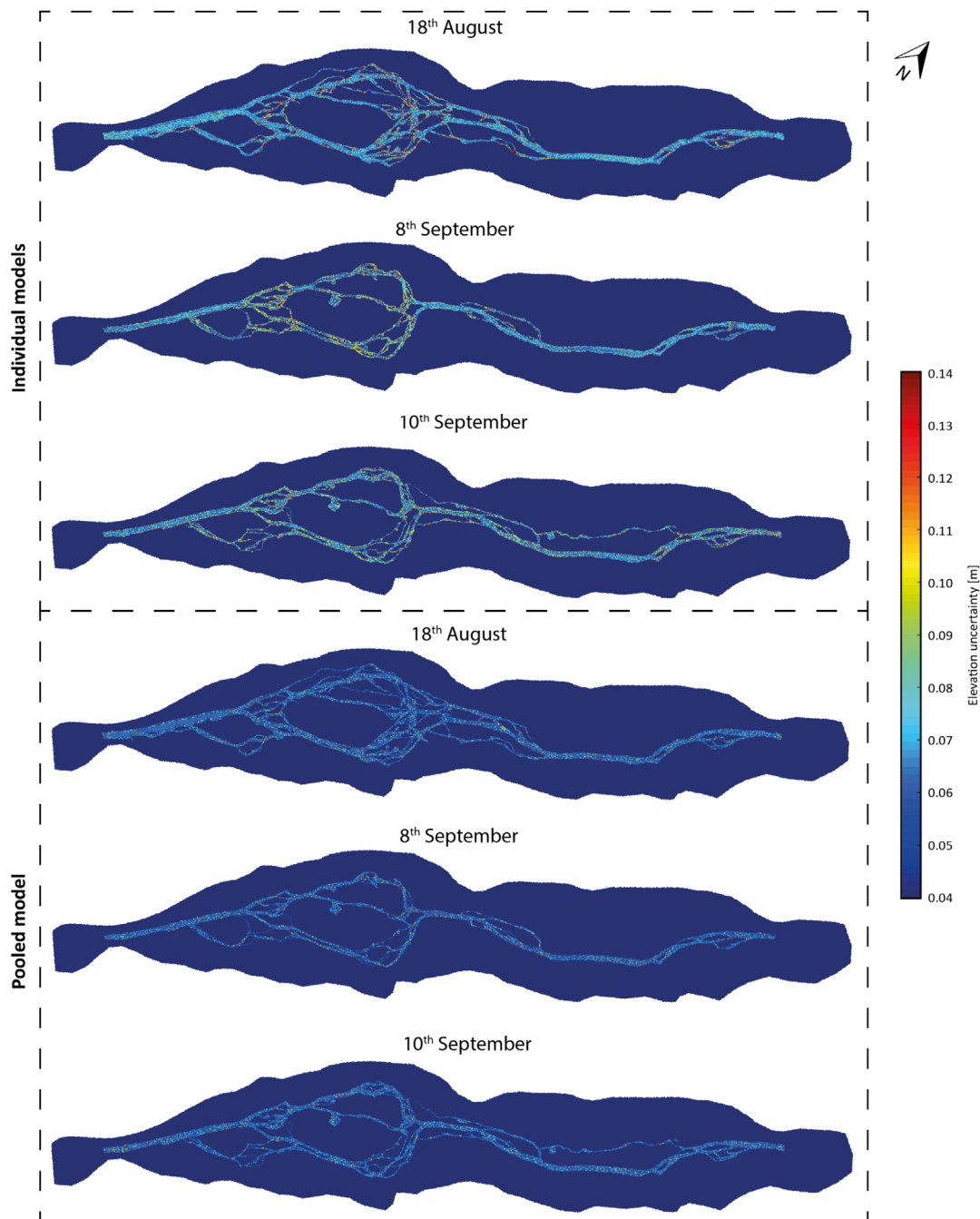


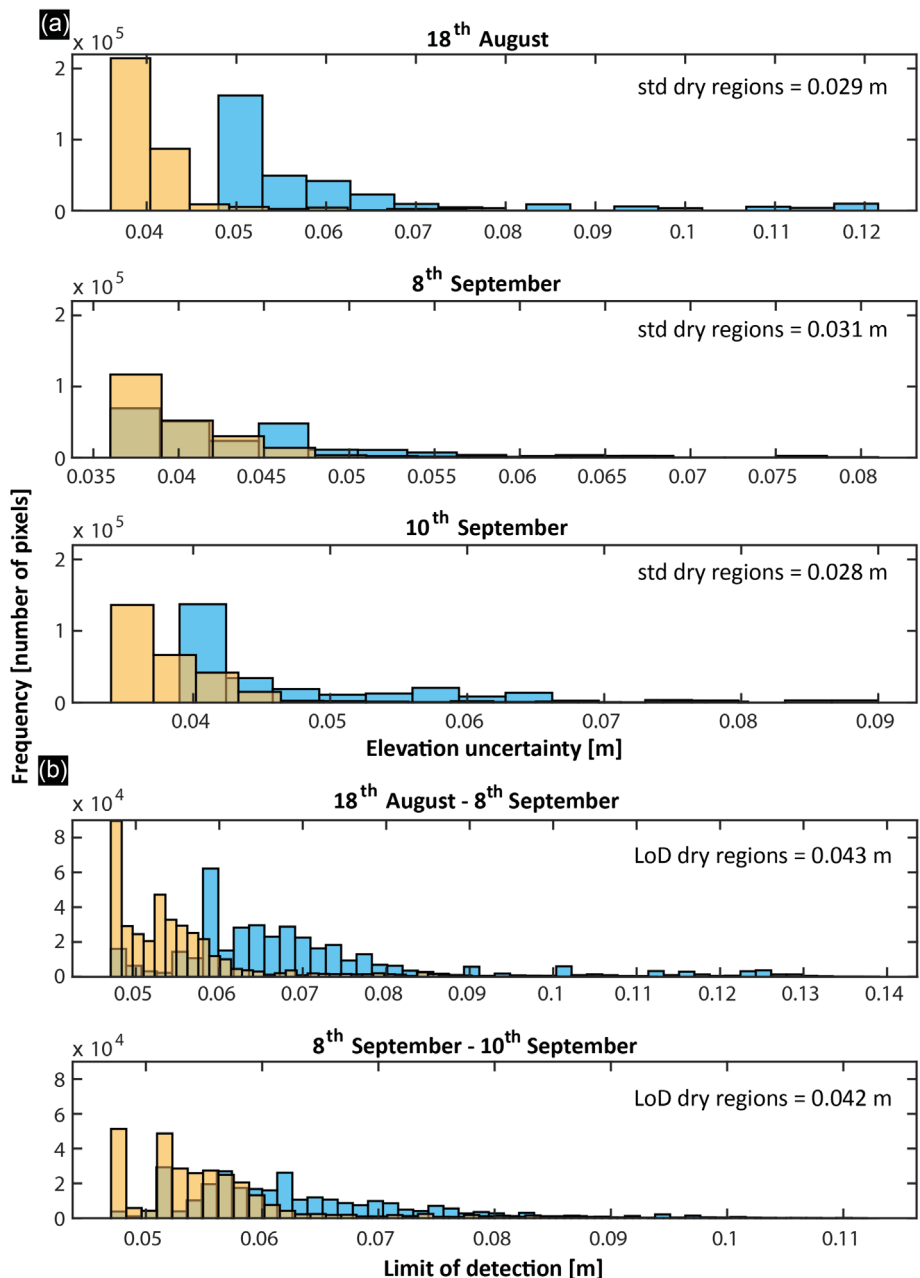
FIGURE 12 Spatial distribution of elevation uncertainty for water depth maps predicted using both individual and pooled models. Dry regions (in dark blue) have lower uncertainties compared to inundated regions.

having shallower depths (Figures 7b and 8c). In the same way, the model for the 10th of September has a better validation R^2 of 0.472 (Figure 7c); albeit with some error remaining, including significant predicted under-estimation, much of it located in the main channel rather than in secondary channels composing the most braided sector (Figure 8d).

The main problem with the individual models is that they have different retained variables and regression coefficients making their application to dates when no calibration data were available a challenge. The pooled calibration approach produced a single model with three predictors (distance from nearest river bank, total inundated width and distance from nearest flow divergence region), a final R^2 value of 0.648 and a SDE of ± 0.113 m (Table 4). Its application using the 2020 datasets produced encouraging results as the validation R^2

values were substantially higher than for individual models (Figure 7) and the residuals had a lower range of magnitude; the R^2 was close to 0.6 for each of the three validation dates, with residual errors of ca. ± 0.1 m (Figure 10 and Table 5). Predictions and residual errors were better for the September datasets than for the August one likely because of the lower flow conditions (Figures 1 and 10a). The distributions of residual error were generally within ± 0.1 m for secondary channels, increasing to ca. -0.4 m to $+0.3$ m in regions characterized by single straight channels (Figure 8). Thus, despite the occurrence of a certain degree of error in the predicted water depths, a multiple linear regression constructed using a greater number of samples collected during different discharge and morphological conditions has a better performance compared to daily models (Table 5; Supplementary Information S6).

FIGURE 13 Histograms of the frequency (i.e. number of cells) for both (a) elevation uncertainty and (b) limits of detection for permanently inundated and transient regions. Light blue refers to results issued using the individual calibrated models, while light orange one to those obtained using the pooled model.



The final water depth distributions resulting from the pooled model make qualitative sense. The study area is composed of three sectors each having different fluvial patterns: a highly braided sector in the middle of the proglacial floodplain bounded by a straight channel configuration upstream towards the glacier terminus and downstream at the forefield end (Figure 1). The pooled model produces water depth distribution maps (Figure 9) that reflect this configuration; water depths are higher for straight stream transects where flow is confined into a single channel, while much lower in the most braided regions (Figure 9). Secondary flow, as represented by channel curvature, does not seem to be important in explaining water depth distributions as no models included it (Tables 3 and 5). A possible explanation could be related to the high ratio of channel width to water depth, which may not be sufficient to allow the development of significant secondary circulation in this system (Nezu et al., 1985).

Water depths are also very heterogeneous in the braided stream sector because of the recurrence of flow divergence and convergence regions (Figures 6 and 9). Previous studies of the morphodynamics of

braided streams show that flow divergence regions are mainly characterized by upstream bar deposition because of flow velocity reduction; in junctions, scouring may occur due to increasing stream power related to an enhancement in flow velocity, also eventually reinforced by secondary circulation if channel geometry permits (e.g. Ashworth, 1996; Lisle et al., 1991; Powell, 1998; Schuurman & Kleinans, 2015).

On this basis, both the quantitative and the qualitative elements sustain the hypothesis that the heuristic-approach presented here can be used to estimate spatially-distributed water depth patterns in a turbid braided stream (Figures 7–10 and Table 5).

4.2 | Use of water depth maps for DEM construction and estimation of change volumes

Incorporation of the bathymetric maps into the dry area DEMs allowed us to create complete DEMs for the three dates and to also produce spatially-explicit maps of elevation uncertainty. For the

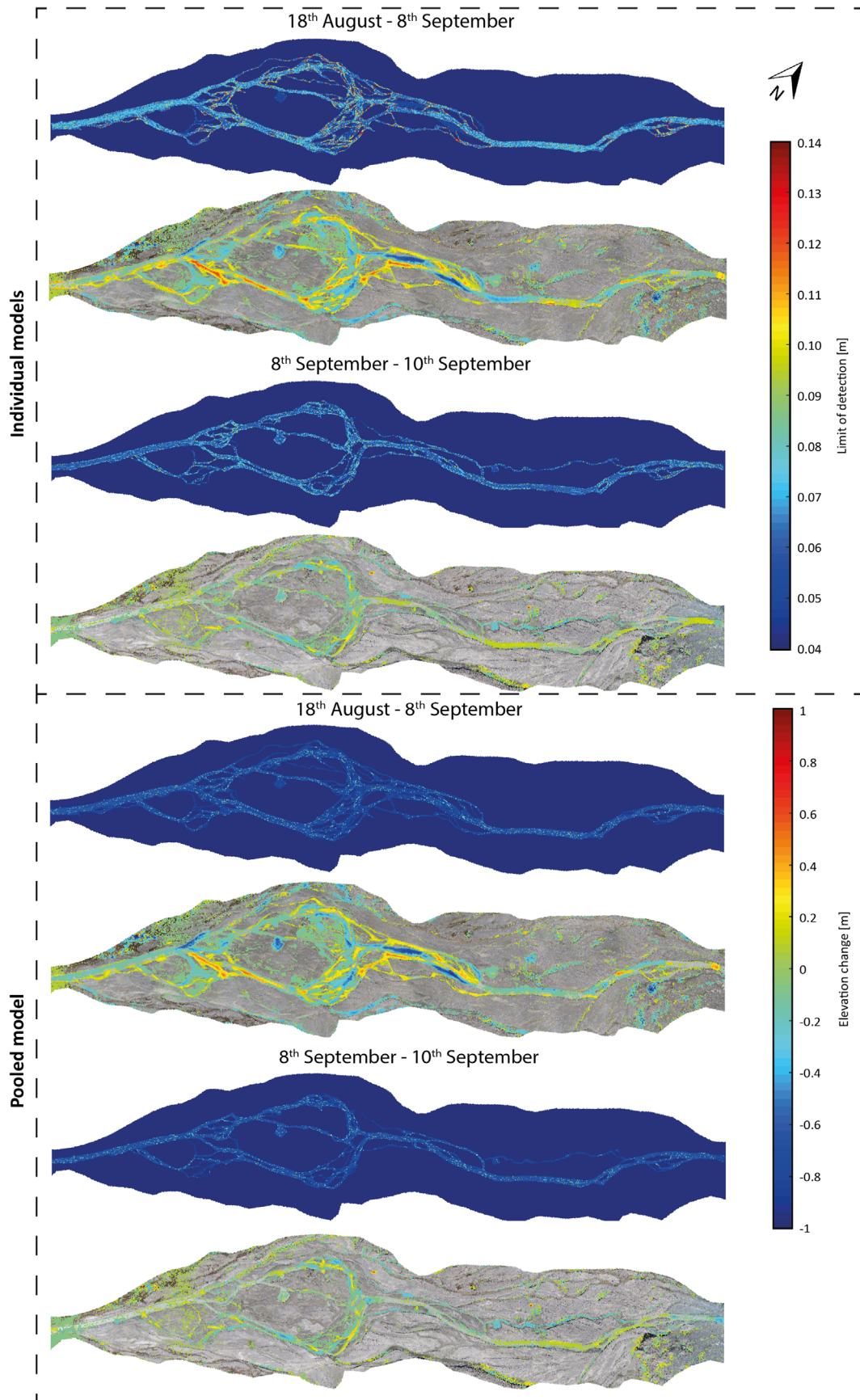


FIGURE 14 Spatial distribution of limits of detection (upper maps) for water depth prediction maps obtained using both individual and pooled models, and associated significant elevation changes (lower maps).

pooled model, elevation uncertainties were ± 0.035 m to ± 0.06 m in all datasets, comparable to the D_{50} of the study area. The resulting levels of detection in permanently inundated areas were between

± 0.045 m and ± 0.09 m. Thus, whilst reworking and deposition patterns could be detected for dry-dry changes that were smaller than the mean D_{50} (i.e. 0.06 m), this rose to $1.5D_{50}$ for wet-wet changes.

Dry-wet and wet-dry changes lie between these two extremes. This is an encouraging result for using these DEMs for change detection and estimation of volumetric change.

Volumetric change estimates suggest that regions permanently dry in both surveys (but that could be inundated between surveys) contributed less to the total volume change over both temporal scales (1.5% to 15.8%, Table 6). Regions permanently wet were those affected by higher reworking over long timescales (37% to 40%, Table 6). Transient regions passing from dry to wet recorded more changes over short timescales (66% to 70%, Table 6). During the investigated period the proglacial forefield experienced a net phase of incision reflected in both long-term (i.e. 18th August to 8th September) and short-term (i.e. 8th September to 10th September) volumetric quantifications.

Cumulative volumetric change estimates highlight different patterns according to the timescale of analysis: over short timescales the cumulative contribution of transient regions is much higher (>80%) compared to permanently wet and permanently dry regions; the latter become dominant (>50%) over longer timescales of analysis. These match previous observations of the importance of transient fluvial regions in braided rivers, such as bars, in acting as both sediment sinks and sources (e.g. Ashmore, 1982; Ashmore, 2013; Ferguson, 1987; Jagers, 2003). In proglacial margins geomorphic changes that occur underwater are not easily taken into account in volumetric change quantifications because high turbidity impedes measurement of underwater topography using current remote sensing approaches (e.g. Beawert & Morche, 2014; Brasington et al., 2012; Milan et al., 2007). As a consequence, this results in significant underestimation of total volumetric estimates.

4.3 | Perspectives for development and application

The errors in depth estimation reported in Table 5 are better than the ±0.15 to ±0.30 m errors reported when applying the Beer–Lambert law

to lower resolution imagery (i.e. Fonstad & Marcus, 2005; Lane et al., 2003; Westaway et al., 2003), and in line with those of ca. ±0.05 m and ±0.10 m issued from the application of two-media photogrammetry approaches (i.e. Dietrich, 2017; Westaway et al., 2001; Woodget et al., 2015). They are much bigger than the ±10 mm obtained with laser scanning (LiDAR) and multi-beam techniques (i.e. Smith & Vericat, 2014). However, the precisions of our results are better than those of Bures et al. (2019), where authors reported errors up to ±0.30 m, involving a comparable method based on morphometric variables to predict cross-sectional water depths in meandering streams.

Model sensitivities and errors for representing riverbed topography are likely dependent on other factors in addition to sampling strategy, including survey instrument precision, survey point quality, surface complexity and roughness, grid resolution and interpolation method (Bangen et al., 2016; Lane, 1998; Lane et al., 1994). These affect water depth maps to different degrees irrespective of the used model. However, increasing the total amount of measured water depths during the calibration process and paying attention to their spatial distribution (i.e. main and secondary channels; depth ranges) seems to be of major importance (Lane, 1998). Further analyses have to be done in this regard, but testing of the model according to the above-proposed conditions can be limited by the feasibility of collecting water depth measurements in deeper areas and during periods of relatively constant discharge.

The proposed methodology does not take into account the effects of bedforms smaller than bars on the riverbed, such as sand and gravel ripples or dunes and riffle-pool sequences, on water depth distribution (Dhont & Ancey, 2018; Gomez et al., 1989; Venditti et al., 2017). Such features are typical of alluvial rivers flowing on mobile beds (Cartigny et al., 2013). They may be between a few and 10s of centimetres in height in this kind of stream, even if normally always smaller than channel-scale bar forms (Dey, 2014; Venditti et al., 2017). Such bedforms have a riverbed bathymetric expression largely independent of the surficial planimetric configuration of the

TABLE 6 Volumetric change estimates [m³] in dry, inundated and transient (i.e. dry to wet and wet to dry) regions issued from DoD maps involving DEMs of both dry and wet areas (Figure 14).

Model	Period	Total volumetric change [m ³]	Sectorial volumetric change [m ³]			
			Before		After	
			Wet	Dry	Wet	Dry
individual	18th August - 9th September	3.322 × 10 ³	-1,374 (37.4%)	-710.3 (21.4%)	Wet	
			1,011 (26.4%)	-434.2 (15.8%)		Dry
	9th September - 10th September	555.2	-66.07 (11.9%)	-366.2 (66.0%)	Wet	
			114.6 (20.6%)	-8.438 (-1.5%)		Dry
Pooled	18th August - 9th September	3.436 × 10 ³	-1,374 (40.0%)	-724.1 (21.1%)	Wet	
			903.8 (26.3%)	-434.2 (12.6%)		Dry
	9th September - 10th September	557.3	-49.23 (8.8%)	-389.2 (69.8%)	Wet	
			110.32 (19.8%)	-8.605 (1.5%)		Dry

channel and so are not modelled in our study (Carling, 1999; Carling et al., 2005). These structures are likely to explain a certain degree of error between predicted and measured water depths, especially in secondary channels because of their higher sensitivity to the transition from subcritical to critical flow conditions (Figures 8 and 10).

That said, despite these sources of uncertainties, both individual and pooled prediction models scale predicted water depths by discharge conditions (i.e. higher predicted water depths for datasets collected at higher flow conditions; Figures 6 and 9).

Even if the results are encouraging, the model still suffers from methodological issues resulting in local large errors (Supplementary Material S7). To improve the overall reliability of the predictions, three improvements merit attention. First, as mentioned above, particular attention should be given to the field sampling strategy for collecting water depth measurements as it needs to take into account both shallow (i.e. secondary channels) and deep (i.e. the main channel) reaches of the investigated area for calibration. This may increase the number of variables retained in the multiple linear regressions, and/or improve the predictive capacity of the model. Second, adding more generic topographic and hydraulic variables (i.e. valley bottom slope distribution, local flow velocity, ...) to the initial pool of variables could be beneficial to expand the number of factors that can potentially explain water depth distribution in the stepwise approach. Combining the proposed model with another one specifically designed for water depth prediction in straight channels might merit consideration. Third, the detection of random errors in water depth prediction maps could be investigated by computing the continuous slope between inundated cells. If the slope within two boundary cells exceeds a given threshold, the local water depth could be considered erroneous. Finally, further improvements may be made to fully automate the algorithm, although the degree of manual correction needed is relatively restricted (i) to the classification of turbid water to produce inundated maps and (ii) to locate flow divergence and convergence regions.

The future application of outputs obtained from the application of our approach is not only limited to the quantification of topographic change estimation. The geometrical analyses here go further than the analysis of stream nodes and links of Hiatt et al. (2019), notably in terms of curvature and convergence/divergence estimation, but also wider parameters related to braided rivers and their ecosystems. For instance, data from these analyses have been used to show how braided river morphodynamics condition the access to water for embryonic vegetation succession, notably linked to biofilm development (Roncoroni, Mancini, Miesen, Müller, et al., 2023). Spatial patterns of water depth and bed elevation are also central to hydraulic modelling whether for understanding spatially-distributed patterns of sediment transport using morphological (e.g. Antoniazza et al., 2019) or hydraulic (e.g. Reid et al., 2019; Williams et al., 2016) modelling and habitat analysis (e.g. Gabbud et al., 2019).

5 | CONCLUSIONS

This study addressed the question of whether the spatial distribution of water depths of shallow braided mountain streams can be estimated based on five basic planimetric variables derived from heuristic statements of what might influence that distribution. We tested this for

three individual datasets for summer 2020, as well as for a pooled model for all datasets. We used a split calibration-validation approach. Results showed that the proposed methodology is promising for obtaining reliable predictions, especially in proglacial streams where the application of remote sensing techniques (e.g. two-media photogrammetry, optical methods) is not suitable due to the high turbidity contents. Using models calibrated using different total water depth measurements and spatial distributions within main and secondary channels produced different results, we observed that the robustness of, and the variables included in, the models appear to be dependent upon survey design. That said, the pooled model involving all datapoints collected in the three datasets gave better results than individual models. However, regardless of the approach used to calibrate the predictive model, the obtained bathymetric maps respect discharge conditions and the basics hydraulic theories, in particular those related to hydraulic geometry and erosion and deposition patterns associated with, respectively, flow divergence and convergence regions.

In the same way, volumetric change estimates computed by integrating water depth maps into DEMs of dry regions suggest that a large proportion of geomorphic changes in these environments occur both underwater and in transient (i.e. zones passing from wet to dry, or vice-versa) zones. However, cumulative effects on the total volumetric change depend on the timescale under investigation: over long temporal scales stable regions contribute the most, while over short timescales are the transient ones which become dominant. These observations highlight the need for (1) a methodological approach to quantify volumetric changes in flooded areas situated in proglacial margins to obtain more reliable quantifications, but also (2) careful consideration of the validity of the proposed statistical approach for bathymetric mapping in turbid braided streams.

AUTHOR CONTRIBUTIONS

Mancini, D: Conceptualization; methodology; investigation; software; writing—initial draft; writing—reviewing and editing. **Antoniazza, G:** Conceptualization; investigation; writing—reviewing and editing. **Roncoroni, M:** Conceptualization; investigation; writing—reviewing and editing. **Mettra, F:** Conceptualization; investigation; writing—reviewing and editing. **Lane, SN.:** Conceptualization; methodology; investigation; funding acquisition; methodology; software; supervision; writing—reviewing and editing.

ACKNOWLEDGEMENTS

This work was supported by the Fondation Agassiz of the Université de Lausanne and by the Swiss National Science Foundation (SNSF) grant N°200021_188734 awarded to S. Lane. The authors are grateful to Gianini, M., Ouvry, B., Lardet, F. and Selitaj, A. for their help during the data collection, and also to the authorities of the Commune de Bagnes and of the Canton du Valais for granting access to the field site for the entire duration of the study. Three anonymous reviewers are also thanked for their constructive comments on a previous version of this manuscript.

DATA AVAILABILITY STATEMENT

The data used in this study (i.e. DEMs, measured water depths used for both model calibration and validation processes and the bathymetric model) are currently in the way to be archived in Zenodo. The authors are aware that data have to be accessible by the time

the manuscript is accepted for publication. A proper and complete reference disposing of a DOI will be given by that time. Other data used in this study (i.e. 2020 orthomosaics) are already archived in Zenodo and properly mentioned in the main text as Roncoroni, Mancini, and Miesen (2023).

ORCID

Davide Mancini  <https://orcid.org/0000-0003-4022-4351>

Gilles Antoniazza  <https://orcid.org/0000-0002-0394-3237>

Matteo Roncoroni  <https://orcid.org/0000-0001-6957-6225>

François Mettra  <https://orcid.org/0000-0001-7423-6444>

Stuart N. Lane  <https://orcid.org/0000-0002-6077-6076>

REFERENCES

- Almeida, T.G., Walker, D.T. & Warnock, A.M. (2017) Estimating river bathymetry from surface velocity observations using Variational inverse modeling. *Journal of Atmospheric and Oceanic Technology*, 35(1), 21–34. Available from: <https://doi.org/10.1175/JTECH-D-17-0075.1>
- Antoniazza, G., Bakker, M. & Lane, S.N. (2019) Revisiting the morphological method in two-dimensions to quantify bed-material transport in braided rivers. *Earth Surface Processes and Landforms*, 44(11), 2251–2267. Available from: <https://doi.org/10.1002/esp.4633>
- Ashmore, P.E. (1982) Laboratory modelling of gravel braided stream morphology. *Earth Surface Processes and Landforms*, 7(3), 201–225. Available from: <https://doi.org/10.1002/esp.3290070301>
- Ashmore, P.E. (1988) Bed load transport in braided gravel-bed stream models. *Earth Surface Processes and Landforms*, 13(8), 677–695. Available from: <https://doi.org/10.1002/esp.3290130803>
- Ashmore, P.E. (2013) Morphology and dynamics of braided rivers. In: Shroder, J. & Wohl, E. (Eds.) *Treatise on geomorphology*. San Diego: Academic Press, pp. 289–312. Available from: <https://doi.org/10.1016/B978-0-12-374739-6.00242-6>
- Ashmore, P.E., Ferguson, R.I., Prestergaard, K.L., Ashworth, P.J. & Paola, C. (1992) Secondary flow in anabranch confluences of a braided, gravel-bed stream. *Earth Surface Processes and Landforms*, 17(3), 299–311. Available from: <https://doi.org/10.1002/esp.3290170308>
- Ashworth, P.J. (1996) Mid-Channel Bar growth and its relationship to local flow strength and direction. *Earth Surface Processes and Landforms*, 21(2), 103–123. Available from: [https://doi.org/10.1002/\(SICI\)1096-9837\(199602\)21:2<103::AID-ESP569>3.0.CO;2-O](https://doi.org/10.1002/(SICI)1096-9837(199602)21:2<103::AID-ESP569>3.0.CO;2-O)
- Bangen, S., Hensleigh, J., McHugh, P. & Wheaton, J. (2016) Error modeling of DEMs from topographic surveys of rivers using fuzzy inference systems. *Water Resources Research*, 52(2), 1176–1193. Available from: <https://doi.org/10.1002/2015WR018299>
- Bangen, S.G., Wheaton, J.M., Bouwes, N., Bouwes, B. & Jordan, C. (2014) A methodological intercomparison of topographic survey techniques for characterizing wadeable streams and rivers. *Geomorphology*, 206, 343–361. Available from: <https://doi.org/10.1016/j.geomorph.2013.10.10>
- Beawert, H. & Morche, D. (2014) Coarse sediment dynamics in a proglacial fluvial system (Fagge River, Tyrol). *Geomorphology*, 218(88), 97–97. Available from: <https://doi.org/10.1016/j.geomorph.2013.10.021>
- Begin, Z.B. (1981) Stream curvature and Bank erosion: a model based on the momentum equation. *The Journal of Geology*, 89(4), 497–504. Available from: <https://doi.org/10.1086/628610>
- Best, J.L. (1988) Sediment transport and bed morphology at river channel confluences. *Sedimentology*, 35(3), 481–498. Available from: <https://doi.org/10.1111/j.1365-3091.1988.tb00999.x>
- Best, J.L. & Reid, I. (1984) Separation zone at Open-Channel junctions. *Journal of Hydraulic Engineering*, 110(11), 1588–1594. Available from: [https://doi.org/10.1061/\(ASCE\)0733-9429\(1984\)110:11\(1588\)](https://doi.org/10.1061/(ASCE)0733-9429(1984)110:11(1588))
- Brasington, J., Langham, J. & Rumsby, B. (2003) Methodological sensitivity of morphometric estimates of coarse fluvial sediment transport. *Geomorphology*, 53(3), 299–316. Available from: [https://doi.org/10.1016/S0169-555X\(02\)00320-3](https://doi.org/10.1016/S0169-555X(02)00320-3)
- Brasington, J., Rumsby, B.T. & McVey, R.A. (2000) Monitoring and modelling morphological change in a braided gravel-bed river using high resolution GPS-based survey. *Earth Surface Processes and Landforms*, 25(9), 973–990. Available from: [https://doi.org/10.1002/1096-9837\(200008\)25:9<973::AID-ESP111>3.0.CO;2-Y](https://doi.org/10.1002/1096-9837(200008)25:9<973::AID-ESP111>3.0.CO;2-Y)
- Brasington, J., Vericat, D. & Rychkov, I. (2012) Modeling river bed morphology, roughness, and surface sedimentology using high resolution terrestrial laser scanning. *Water Resources Research*, 48(11), W11519. Available from: <https://doi.org/10.1029/2012WR012223>
- Breaux, H.J. (1967) *On stepwise multiple linear regression (Report No. 1369)*. Aberdeen Proving Ground, Maryland: U.S. Army Material Command, Ballistic Research Laboratories.
- Brice, J.C. (1975) *Airphoto interpretation of the form and behavior of alluvial rivers (ADA008108)*. Washington University, St. Louis: U.S. Army Research Office.
- Bristow, C.S. & Best, J.L. (1993) Braided rivers: perspectives and problems. *Geological Society, London, Special Publications*, 75(1), 1–11. Available from: <https://doi.org/10.1144/GSL.SP.1993.075.01.01>
- Bures, L., Sychova, P., Maca, P., Roub, R. & Marval, S. (2019) River bathymetry model based on floodplain topography. *Water*, 11(6), 1287. Available from: <https://doi.org/10.3390/w11061287>
- Carbonneau, P.E. & Dietrich, J.T. (2017) Cost-effective non-metric photogrammetry from consumer-grade sUAS: implications for direct georeferencing of structure from motion photogrammetry. *Earth Surface Processes and Landforms*, 42(3), 473–486. Available from: <https://doi.org/10.1002/esp.4012>
- Carling, P.A. (1999) Subaqueous gravel dunes. *Journal of Sedimentary Research*, 69(3), 534–545. Available from: <https://doi.org/10.2110/jsr.69.534>
- Carling, P.A., Richardson, K. & Ikeda, H. (2005) A flume experiment on the development of subaqueous fine gravel dunes from a lower stage plane bed. *Journal of Geophysical Research: Earth Surface*, 110(F4), F04S05. Available from: <https://doi.org/10.1029/2004JF000205>
- Carrivick, J.L. & Heckmann, T. (2017) Short-term geomorphological evolution of proglacial systems. *Geomorphology*, 287, 3–28. Available from: <https://doi.org/10.1016/j.geomorph.2017.01.037>
- Cartigny, M.J.B., Ventra, D., Postma, G. & van Den Berg, J. (2013) Morphodynamics and sedimentary structure of bedforms under supercritical-flow conditions: new insights from flume experiments. *Sedimentology*, 61(3), 712–748. Available from: <https://doi.org/10.1111/sed.12076>
- Chandler, J., Ashmore, P., Paola, C., Gooch, M. & Varkaris, F. (2002) Monitoring river-channel change using terrestrial oblique imagery and automated digital photogrammetry. *Annals of the Association of American Geographers*, 92(4), 631–644. Available from: <https://doi.org/10.1111/1467-8306.00308>
- Dey, S. (2014) Bedforms. In: Dey, S. (Ed.) *Fluvial hydrodynamics: hydrodynamics and sediment transport phenomena*. Heidelberg: Springer. Available from: https://doi.org/10.1007/978-3-642-19062-9_8
- Dhont, B. & Ancey, C. (2018) Are bedload transport processes pulses in gravel bed rivers created by bar migration or sediment waves? *Geophysical Research Letters*, 45(11), 5501–5508. Available from: <https://doi.org/10.1029/2018GL077792>
- Dietrich, J.T. (2017) Bathymetric structure-from-motion: extracting shallow stream bathymetry from multi-view stereo photogrammetry. *Earth Surface Processes and Landforms*, 42(2), 355–364. Available from: <https://doi.org/10.1002/esp.4060>
- Draper, N.R., & Smith, H. (1998). *Applied regression analysis* (3th edition). New York: Wiley. Available from: <https://doi.org/10.1002/9781118625590>
- Eltner, A., Baumgart, P., Maas, H.G. & Faust, D. (2015) Multi-temporal UAV data for automatic measurement of rill and interrill erosion on loess soil. *Earth Surface Processes and Landforms*, 40(6), 255–274. Available from: <https://doi.org/10.1002/esp.3673>
- Farina, G., Alvisi, S., Franchini, M., Corato, G. & Moramarco, T. (2015) Estimation of bathymetry (and discharge) in natural river cross-sections by using an entropy approach. *Journal of Hydrology*, 527, 20–29. Available from: <https://doi.org/10.1016/j.jhydrol.2015.04.037>
- Ferguson, R.I. (1987) Hydraulic and sedimentary controls of channel pattern. In: Richards, K. (Ed.) *River channels: environment and processes*.

- Oxford: The Institute of British Geographers, Blackwell, pp. 129–158.
- Flener, C. (2013) Estimating deep water radiance in shallow water: adapting optical bathymetry modelling to shallow river environments. *Boreal Environment Research*, 18, 488–502.
- Flener, C., Vaaja, M., Jaakkola, A., Krooks, A., Kaartinen, H., Kukko, A., et al. (2013) Seamless mapping of river channels at high resolution using Mobile LiDAR and UAV-photography. *Remote Sensing*, 5(12), 6382–6407. Available from: <https://doi.org/10.3390/rs5126382>
- Fonstad, M.A. & Marcus, W.A. (2005) Remote sensing of stream depths with hydraulically assisted bathymetry (HAB) models. *Geomorphology*, 72(1–4), 320–339. Available from: <https://doi.org/10.1016/j.geomorph.2005.06.005>
- Frascati, A. & Lanzoni, S. (2009) Morphodynamic regime and long-term evolution of meandering rivers. *Journal of Geophysical Research: Earth Surface*, 144. Available from: <https://doi.org/10.1029/2008JF001101>
- Frascati, A. & Lanzoni, S. (2013) A mathematical model for meandering rivers with varying width. *Journal of Geophysical Research: Earth Surface*, 118(3), 1641–1657. Available from: <https://doi.org/10.1002/jgrf.20084>
- Gabbud, C., Bakker, M., Cléménçon, M. & Lane, S.N. (2019) Hydropower Flushing events causes severe loss of Macrozoobenthos in Alpine streams. *Water Resources Research*, 55(12), 10056–10081. Available from: <https://doi.org/10.1029/2019WR024758>
- Gao, M., Tian, J., Ai, L. & Zhang, F. (2008) Sewage Image Feature Extraction and Turbidity Degree Detection Based on Embedded System. In: *2008 international conference on MultiMedia and information technology, Three Gorges, China*. IEEE, pp. 357–360. Available from: <https://doi.org/10.1109/MMIT.2008.196>
- Gilvear, D.J., Waters, T.M. & Milner, A.M. (1995) Image analysis of aerial photography to quantify changes in channel morphology and instream habitat following placer mining in interior Alaska. *Freshwater Biology*, 34(2), 389–398. Available from: <https://doi.org/10.1111/j.1365-2427.1995.tb00897.x>
- Gilvear, D.J., Waters, T.M. & Milner, A.M. (1998) Image analysis of aerial photography to quantify the effect of gold placer mining on channel morphology, interior Alaska. In: Lane, S.N., Richards, K.S. & Chandler, J.H. (Eds.) *Landform monitoring, modelling and analysis*. London: Wiley, pp. 195–216.
- Gomez, B., Naff, R.L. & Hubbell, D.W. (1989) Temporal variation in bedload transport rates associated with the migration of bedforms. *Earth Surface Processes and Landforms*, 14(2), 135–156. Available from: <https://doi.org/10.1002/esp.329014025>
- Hiatt, M., Sonke, W., Addink, E.A., van Dijk, W.M., van Kreveld, M., Ophelders, T., et al. (2019) Geometry and topology of estuary and Braided River channel networks automatically extracted from topographic data. *Journal of Geophysical Research: Earth Surface*, 125(1), e2019JF005206. Available from: <https://doi.org/10.1029/2019JF005206>
- Hicks, D.M. (2012) Remotely sensed topographic change in gravel riverbeds with flowing channels. In: Church, M., Biron, P. & Roy, A. (Eds.) *Gravel-bed Rivers: processes, tools, environments*. Chichester: Wiley. Available from: <https://doi.org/10.1002/9781119952497.ch23>
- Hugenholtz, C.H., Whitehead, K., Brown, O.W., Barchyn, T.E., Moorman, B.J., Le Clair, A., et al. (2013) Geomorphological mapping with a small unmanned aircraft system (sUAS): feature detection and accuracy assessment of a photogrammetrically-derived digital terrain model. *Geomorphology*, 194, 16–24. Available from: <https://doi.org/10.1016/j.geomorph.2013.03.023>
- Jagers, H.R.A. (2003) *Modelling planform changes of braided rivers*. Ph.D. thesis. Twente, The Netherlands: University of Twente.
- James, G., Witten, D., Hastie, T. & Tibshirani, R. (2013) Linear Regression. In: James, G., Witten, D., Hastie, T. & Tibshirani, R. (Eds.) *An Introduction to statistical learning: with applications in R*. New York: Springer, pp. 59–126. Available from: https://doi.org/10.1007/978-1-4614-7138-7_3
- James, M.R., Antoniazza, G., Robson, S. & Lane, S.N. (2020) Mitigating systematic error in topographic models for geomorphic change detection: accuracy, precision and considerations beyond off-nadir imagery. *Earth Surface Processes and Landforms*, 45(10), 2251–2271. Available from: <https://doi.org/10.1002/esp.4878>
- James, M.R., Robson, S., d'Oleire-Oltmanns, S. & Niethammer, U. (2017) Optimising UAV topographic surveys processed with structure-from-motion: ground control quality, quantity and bundle adjustment. *Geomorphology*, 280, 51–66. Available from: <https://doi.org/10.1016/j.geomorph.2016.11.021>
- James, M.R., Robson, S. & Smith, M.W. (2017) 3-D uncertainty-based topographic change detection with structure-from-motion photogrammetry: precision maps for ground control and directly georeferenced surveys. *Earth Surface Processes and Landforms*, 42(12), 1769–1788. Available from: <https://doi.org/10.1002/esp.4125>
- Kasvi, E., Salmela, J., Lotsari, E., Kumpula, T. & Lane, S.N. (2019) Comparison of remote sensing based approaches for mapping bathymetry of shallow, clear water rivers. *Geomorphology*, 333, 180–197. Available from: <https://doi.org/10.1016/j.geomorph.2019.02.017>
- Lane, S.N. (1998) The use of digital terrain modelling in the understanding of dynamic river channel systems. In: Lane, S.N., Richards, K.S. & Chandler, J.H. (Eds.) *Landform monitoring, modelling and analysis*. London: Wiley, pp. 311–342.
- Lane, S.N., Gentile, A. & Goldenschue, L. (2020) Combining UAV-based SfM-MVS photogrammetry with conventional monitoring to set environmental flows: modifying dam Flushing flows to improve Alpine stream habitat. *Remote Sensing*, 12(23), 3868. Available from: <https://doi.org/10.3390/rs12233868>
- Lane, S.N., Richards, K.S. & Chandler, J.H. (1994) Developments in monitoring and modelling small-scale river bed topography. *Earth Surface Processes and Landforms*, 19(4), 349–368. Available from: <https://doi.org/10.1002/esp.3290190406>
- Lane, S.N., Westaway, R.M. & Hicks, M.D. (2003) Estimation of erosion and deposition volumes in a large, gravel-bed, braided river using synoptic remote sensing. *Earth Surface Processes and Landforms*, 28(3), 249–271. Available from: <https://doi.org/10.1002/esp.483>
- Lane, S.N., Widdison, P.E., Thomas, R.E., Ashworth, P.J., Best, J.L., Lunt, I.A., et al. (2010) Quantification of braided river channel change using archival digital image analysis. *Earth Surface Processes and Landforms*, 35(8), 971–985. Available from: <https://doi.org/10.1002/esp.2015>
- Legleiter, C.J. & Roberts, D.A. (2005) Effects of channel morphology and sensor spatial resolution on image-derived depth estimates. *Remote Sensing of Environment*, 95(2), 231–247. Available from: <https://doi.org/10.1016/j.rse.2004.12.013>
- Legleiter, C.J., Roberts, D.A., Marcus, W.A. & Fonstad, M.A. (2004) Passive optical remote sensing of river channel morphology and in-stream habitat: physical basis and feasibility. *Remote Sensing of Environment*, 93(4), 493–510. Available from: <https://doi.org/10.1016/j.rse.2004.07.019>
- Leopold, L.B. & Maddock, T. (1953) *The hydraulic geometry of stream channels and some physiographic implications (USGS numbered series 252)*. Washington D.C.: U.S. Government Printing Office.
- Lisle, T.E., Ikeda, H. & Iseya, F. (1991) Formation of stationary alternate bars in a steep channel with mixed-size sediment: a flume experiment. *Earth Surface Processes and Landforms*, 16(5), 463–469. Available from: <https://doi.org/10.1002/esp.3290160507>
- Liu, Y., Chen, Y. & Fang, X. (2018) A review of turbidity detection based on computer vision. *IEEE Access*, 6, 60586–60604. Available from: <https://doi.org/10.1109/ACCESS.2018.2875071>
- Mackin, J. (1948) Concept of the graded river. *Geological Society of America Bulletin*, 59(5), 463–511. Available from: [https://doi.org/10.1130/0016-7606\(1948\)59\[463:COTGR\]2.0.CO;2](https://doi.org/10.1130/0016-7606(1948)59[463:COTGR]2.0.CO;2)
- Maddock, I. (1999) The importance of physical habitat assessment for evaluating river health. *Freshwater Biology*, 41(2), 373–391. Available from: <https://doi.org/10.1046/j.1365-2427.1999.00437.x>
- Mancini, D., Antoniazza, G., Roncoroni, M., Mettra, F. & Lane, S.N. (2024). Heuristic estimation of river bathymetry in braided streams using digital image processing: model workflow (Version 1). Zenodo. Available from: <https://doi.org/10.5281/zenodo.12720137>
- Mancini, D. & Lane, S.N. (2020) Changes in sediment connectivity following glacial debuitting in an Alpine Valley system. *Geomorphology*,

- 352, 106987. Available from: <https://doi.org/10.1016/j.geomorph.2019.106987>
- Marcus, W.A. & Fonstad, M.A. (2008) Optical remote mapping of rivers at sub-meter resolutions and watershed extents. *Earth Surface Processes and Landforms*, 33(1), 4–24. Available from: <https://doi.org/10.1002/esp.1637>
- Marcus, W.A., Fonstad, M.A. & Legleiter, C.J. (2012) Management applications of optical remote sensing in the active river channel. In: Carbonneau, P.E. & Piegay, H. (Eds.) *Fluvial remote sensing for science and management*. Chichester: Wiley-Blackwell. Available from: <https://doi.org/10.1002/9781119940791.ch2>
- Marcus, W.A., Legleiter, C.J., Aspinall, R.J., Boardman, J.W. & Crabtree, R.L. (2003) High spatial resolution hyperspectral mapping of in-stream habitats, depths, and woody debris in mountain streams. *Geomorphology*, 55(1), 363–380. Available from: [https://doi.org/10.1016/S0169-555X\(03\)00150-8](https://doi.org/10.1016/S0169-555X(03)00150-8)
- Maxwell, A.E. (1975) Limitations on the use of the multiple linear regression model. *British Journal of Mathematical and Statistical Psychology*, 28(1), 51–62. Available from: <https://doi.org/10.1111/j.2044-8317.1975.tb00547.x>
- Mersel, M.K., Smith, L.C., Andreadis, K.M. & Durand, M.T. (2013) Estimation of river depth from remotely sensed hydraulic relationships. *Water Resources Research*, 49(6), 3165–3179. Available from: <https://doi.org/10.1002/wrcr.20176>
- Milan, D.J., Heritage, G.L. & Hetherington, D. (2007) Application of a 3D laser scanner in the assessment of erosion and deposition volumes and channel change in a proglacial river. *Earth Surface Processes and Landforms*, 31(11), 1474–1657. Available from: <https://doi.org/10.1002/esp.1592>
- Mjaavatten, A. (2020). *Curvature of a 1D curve in a 2D or 3D space* (<https://www.mathworks.com/matlabcentral/fileexchange/69452-curvature-of-a-1d-curve-in-a-2d-or-3d-space>), MATLAB Central File Exchange. Retrieved September 4, 2020.
- Mosley, M.P. (1983) Response of braided rivers to changing discharge. *Journal of Hydrology (New Zealand)*, 22(1), 18–67.
- Müller, T., & Miesen, F. (2022). *Stream discharge, stage, electrical conductivity & temperature dataset from Otemma glacier forefield, Switzerland (from July 2019 to October 2021) (v1.2021.02) [dataset]*. Zenodo. Available from: <https://doi.org/10.5281/zenodo.6202732>
- Netter, J., Kutner, M.H. & Wasserman, W. (1983) *Applied linear regression models*. Homewood: McGraw-Hill Higher Education.
- Nezu, I., Nakagawa, H. & Tominaga, A. (1985) Secondary Currents in a Straight Channel Flow and the Relation to Its Aspect Ratio. In: Bradbury, L.J.S., Durst, F., Launder, B.E., Schmidt, F.W. & Whitelaw, J.H. (Eds.) *Turbulent shear flows*, Vol. 4. Berlin: Springer, pp. 246–260. Available from: https://doi.org/10.1007/978-3-642-69996-2_20
- Niethammer, U., Rothmund, S., James, M.R., Travelletti, J. & Joswig, M. (2010) UAV-based remote sensing of landslides. *International Archives of Photogrammetry, Remote Sensing, and Spatial Information Sciences*, 38, 496–501.
- Olsen, A.A., McLaughlin, J.E. & Harpe, S.E. (2020) Using multiple linear regression in pharmacy education scholarship. *Currents in Pharmacy Teaching and Learning*, 12(10), 1258–1268. Available from: <https://doi.org/10.1016/j.cptl.2020.05.017>
- Ouedraogo, M.M., Degre, A., Debouche, C. & Lisein, J. (2014) The evaluation of unmanned aerial system-based photogrammetry and terrestrial laser scanning to generate DEMs of agricultural watersheds. *Geomorphology*, 214, 339–355. Available from: <https://doi.org/10.1016/j.geomorph.2014.02.016>
- Parker, G., Shimizu, Y., Wilkerson, G.V., Eke, E.C., Abad, J.D., Lauer, J.W., et al. (2011) A new framework for modeling the migration of meandering rivers. *Earth Surface Processes and Landforms*, 36(1), 70–86. Available from: <https://doi.org/10.1002/esp.2113>
- Phillips, J.D. (2003) Sources of nonlinearity and complexity in geomorphic systems. *Progress in Physical Geography: Earth and Environment*, 27(1), 1–23. Available from: <https://doi.org/10.1191/0309133303pp340ra>
- Powell, D.M. (1998) Patterns and processes of sediment sorting in gravel-bed rivers. *Progress in Physical Geography*, 22(1), 1–32. Available from: <https://doi.org/10.1171/030913339802200101>
- Pratomo, D.L.C., Khomsim, K. & Putranto, D.F.E. (2019) Analysis of the green light penetration from airborne LiDAR bathymetry in shallow water area. *IOP Conference Series: Earth and Environmental Science*, 289(1), 012003. Available from: <https://doi.org/10.1088/1755-1315/389/1/012003>
- Reid, H.E., Williams, R.D., Brierley, G.J., Coleman, S.E., Lamb, R., Rennie, C.D., et al. (2019). Geomorphological effectiveness of floods to rework gravel bars: insight from hyperscale topography and hydraulic modelling. *Earth Surface Processes and Landforms*, 44, 595–613. Available from: <https://doi.org/10.1002/esp.4521>
- Richardson, W.R. & Thorne, C.R. (1988) Secondary currents around braid bar in Brahmaputra River, Bangladesh. *Journal of Hydraulic Engineering*, 124(3), 325–328. Available from: [https://doi.org/10.1061/\(ASCE\)0733-9429\(1998\)124:3\(325\)](https://doi.org/10.1061/(ASCE)0733-9429(1998)124:3(325))
- Roncoroni, M., Mancini, D., Kohler, T.J., Miesen, F., Gianini, M., Battin, T.J., et al. (2022) Centimeter-scale mapping of phototrophic biofilms in glacial forefields using visible band ratios and UAV imagery. *International Journal of Remote Sensing*, 43(13), 4723–4757. Available from: <https://doi.org/10.1080/01431161.2022.2079963>
- Roncoroni, M., Mancini, D., & Miesen, F. (2023). *SfM-MVS derived orthomosaics of the Otemma glacier forefield (2020) (version 1) [dataset]*. Zenodo. Available from: <https://doi.org/10.5281/zenodo.7514935>
- Roncoroni, M., Mancini, D., Miesen, F., Müller, T., Gianini, M., Ouvry, B., et al. (2023) Decrypting the stream periphyton physical habitat of recently deglaciated floodplains. *Science of the Total Environment*, 867, 161374. Available from: <https://doi.org/10.1016/j.scitotenv.2022.161374>
- Rose, K.C., Hamilton, D.P., Williamson, C.E., McBride, C.G., Fischer, J.M., Olson, M.H., et al. (2014) Light attenuation characteristics of glacially-fed lakes. *Journal of Geophysical Research: Biogeosciences*, 119(7), 1446–1457. Available from: <https://doi.org/10.1002/2014JG002674>
- Schaperow, J.R., Li, D., Margulis, S.A. & Lettenmaier, D.P. (2019) A curve-fitting method for estimating bathymetry from water surface height and width. *Water Resources Research*, 55(5), 4288–4303. Available from: <https://doi.org/10.1029/2019WR024938>
- Schuurman, F. & Kleinhans, M.G. (2015) Bar dynamics and bigurcation evolution in a modelled braided sand-bed river. *Earth Surface Processes and Landforms*, 40(10), 1318–1333. Available from: <https://doi.org/10.1002/esp.3722>
- Smith, M.w. & Vericat, D. (2014) Evaluating shallow-water bathymetry from through-water terrestrial laser scanning under a range of hydraulic and physical water quality conditions. *River Research and Applications*, 30(7), 905–924. Available from: <https://doi.org/10.1002/rra.2687>
- Szafarczyk, A. & Tos, C. (2023) The use of green laser in LiDAR bathymetry: state of the art and recent advancements. *Sensors*, 23(1), 292. Available from: <https://doi.org/10.3390/s23010292>
- Tammimga, A., Hugenholtz, C., Eaton, B. & Lapointe, M. (2015) Hyper-spatial remote sensing of channel reach morphology and hydraulic fish habitat using an unmanned aerial vehicle (UAV): a first assessment in the context of river research and management. *River Research and Applications*, 31(3), 379–391. Available from: <https://doi.org/10.1002/rra.2743>
- Tate, N.J., Brundson, C., Charlton, M., Fotheringham, A.S. & Jarvis, C.H. (2005) Smoothing/filtering LiDAR digital surface models. Experiments with low regression and discrete wavelets. *Journal of Geographical Systems*, 7(3–4), 279–290. Available from: <https://doi.org/10.1007/s10109-005-0007-4>
- Thompson, C.G., Kim, R.S., Aloe, A.M. & Becker, B.J. (2017) Extracting the variance inflation factor and other multicollinearity diagnostics from typical regression results. *Basic and Applied Social Psychology*, 39(2), 81–90. Available from: <https://doi.org/10.1080/01973533.2016.1277529>
- Venditti, J.G., Nelson, P.A., Bradley, R.W., Haught, D. & Gitto, A.B. (2017) Bedforms, Structures, Patches and Sediment Supply in Gravel-Bed Rivers. In: Tsutsumi, D. & Laronne, B. (Eds.) *Gravel-bed Rivers: processes and disasters*. Chichester: Wiley. Available from: <https://doi.org/10.1002/9781118971437.ch16>

- Ward, J.V., Tockner, K., Arscott, D.B. & Claret, C. (2002) Riverine landscape diversity. *Freshwater Biology*, 47(4), 517–539. Available from: <https://doi.org/10.1046/j.1365-2427.2002.00893.x>
- Westaway, R.M., Lane, S.N. & Hicks, D.M. (2000) The development of an automated correction procedure for digital photogrammetry for the study of wide, shallow, gravel-bed rivers. *Earth Surface Processes and Landforms*, 25(2), 209–226. Available from: [https://doi.org/10.1002/\(SICI\)1096-9837\(200002\)25:2<209::AID-ESP84>3.0.CO;2-Z](https://doi.org/10.1002/(SICI)1096-9837(200002)25:2<209::AID-ESP84>3.0.CO;2-Z)
- Westaway, R.M., Lane, S.N. & Hicks, D.M. (2001) Remote sensing of clear-water, shallow, gravel-bed rivers using digital photogrammetry. *Photogrammetric Engineering & Remote Sensing*, 67(11), 1271–1281.
- Westaway, R.M., Lane, S.N. & Hicks, D.M. (2003) Remote survey of large-scale braided, gravel-bed rivers using digital photogrammetry and image analysis. *International Journal of Remote Sensing*, 24(4), 795–815. Available from: <https://doi.org/10.1080/01431160110113070>
- Williams, R.D., Measures, R., Hicks, D.M. & Brasington, J. (2016) Assessment of a numerical model to reproduce event-scale erosion and depositions in a braided river. *Water Resource Research*, 52(8), 6621–6642. Available from: <https://doi.org/10.1002/2015WR018491>
- Winterbottom, S.J. & Gilvear, D.J. (1997) Quantification of channel bed morphology in gravel-bed rivers using airborne multispectral imagery and aerial photography. *Regulated Rivers: Research & Management*, 13(6), 489–499. Available from: [https://doi.org/10.1002/\(SICI\)1099-1646\(199711/12\)13:6<489::AID-RRR471>3.0.CO;2-X](https://doi.org/10.1002/(SICI)1099-1646(199711/12)13:6<489::AID-RRR471>3.0.CO;2-X)
- Woodget, A., Carbonneau, P., Visser, F. & Maddock, I. (2015) Quantifying submerged fluvial topography using hyperspatial resolution UAS imagery and structure from motion photogrammetry. *Earth Surface Processes and Landforms*, 40(1), 47–64. Available from: <https://doi.org/10.1002/esp.3613>

SUPPORTING INFORMATION

Additional supporting information can be found online in the Supporting Information section at the end of this article.

How to cite this article: Mancini, D., Antoniazza, G., Roncoroni, M., Mettra, F. & Lane, S.N. (2024) Heuristic estimation of river bathymetry in braided streams using digital image processing. *Earth Surface Processes and Landforms*, 1–24. Available from: <https://doi.org/10.1002/esp.5944>